

## **Algorithm Theoretical Basis Document**

### **Microwave Imager Radiance FCDR**

### **SSM/I Brightness Temperatures**

**DOI: 10.5676/EUM\_SAF\_CM/FCDR\_MWI/V004**

**Microwave Imager Radiance FCDR R4**

**CM-12003**

Reference Number:


**SAF/CM/DWD/ATBD/FCDR\_SSMI**

Issue/Revision Index:

**2.2**

Date:

**2022-01-31**

	<b>Algorithm Theoretical Basis Document</b> <b>Microwave Imager Radiance FCDR R4</b> <b>SSM/I Brightness Temperatures</b>	Doc. No: SAF/CM/DWD/ATBD/FCDR_SSMI Issue: 2.2 Date: 2022-01-31
---	---	--


## Document Signature Table

	Name	Function	Signature	Date
Author	Karsten Fennig	CM SAF Scientist		2022-01-31
Editor	Marc Schröder	Science Coordinator		2022-01-31
Approval	CM SAF Steering Group			
Release	Rainer Hollmann	Project Manager		

## Distribution List


Internal Distribution	
Name	No. Copies
DWD / Archive	1
CM SAF Team	1

External Distribution		
Company	Name	No. Copies
PUBLIC		1

	<b>Algorithm Theoretical Basis Document</b> <b>Microwave Imager Radiance FCDR R4</b> <b>SSM/I Brightness Temperatures</b>	Doc. No: SAF/CM/DWD/ATBD/FCDR_SSMI Issue: 2.2 Date: 2022-01-31
---	---	--

## Document Change Record

Issue/ Revision	Date	DCN No.	Changed Pages/Paragraphs
1.0	2011-11-05	SAF/CM/DWD/ATBD/FCDR_SSMI	First official version.
1.1	2012-04-27	SAF/CM/DWD/ATBD/FCDR_SSMI	Changes after PCR-4
1.2	2012-10-23	SAF/CM/DWD/ATBD/FCDR_SSMI	Updates for DRI-6 <ul style="list-style-type: none"> <li>• Attitude corrections</li> <li>• Non-linearity corrections</li> <li>• Along-scan correction modified</li> </ul>
1.3	2013-01-31	SAF/CM/DWD/ATBD/FCDR_SSMI	Updates following DRI-6
1.4	2017-01-18	SAF/CM/DWD/ATBD/FCDR_SSMI	Update DOI for FCDR MWI R3
2.0	2018-12-10	SAF/CM/DWD/ATBD/FCDR_SSMI	Version for PCR 3.1
2.1	2019-02-05	SAF/CM/DWD/ATBD/FCDR_SSMI	Final version after PCR.
2.2	2022-01-31	SAF/CM/DWD/ATBD/FCDR_SSMI	Version for DRR 3.1

	<b>Algorithm Theoretical Basis Document</b> <b>Microwave Imager Radiance FCDR R4</b> <b>SSM/I Brightness Temperatures</b>	Doc. No: SAF/CM/DWD/ATBD/FCDR_SSMI Issue: 2.2 Date: 2022-01-31
---	---	--

## Applicable documents

Reference	Title	Code / Validity Date
AD 1	Memorandum of Understanding between CM SAF and the Max-Planck Institute for Meteorology and Meteorological Institute, University of Hamburg	1. March 2012
AD 2	Agreement between the European Organisation for the Exploitation of Meteorological Satellites (EUMETSAT) and the Federal Republic of Germany represented by the Deutsche Wetterdienst on the Continuous Development and Operations Phase of a EUMETSAT Satellite Application Facility in Climate Monitoring	1. December 2006
AD 3	CM SAF Product Requirements Document	SAF/CM/DWD/PRD/3.2

## Reference documents

Reference	Title	Code
RD 1	ATBD Fundamental Climate Data Record of SMMR Brightness Temperatures	SAF/CM/DWD/ATBD/FCDR_SMMR/2.2
RD 2	ATBD Fundamental Climate Data Record of SSMIS Brightness Temperatures	SAF/CM/DWD/ATBD/FCDR_SSMIS/2.2
RD 3	Product User Manual Fundamental Climate Data Record of SSM/I Brightness Temperatures	SAF/CM/DWD/PUM/FCDR_SSMI/1.2

## Table of Contents

I	Preface.....	7
1	The EUMETSAT SAF on Climate Monitoring .....	7
2	Introduction .....	8
II	SMMR .....	9
III	SSM/I .....	10
3	Algorithm Overview .....	10
3.1	The SSM/I Instrument.....	10
4	Algorithm Description .....	12
4.1	FCDR data processing .....	12
4.2	Geolocation.....	14
4.2.1	Land mask and sea ice detection .....	15
4.3	SSM/I calibration .....	16
4.4	Applied corrections.....	17
4.4.1	Along-scan correction .....	17
4.4.2	Cold view intrusions.....	18
4.4.3	Hot load intrusions.....	19
4.4.4	F10 Digital Count Anomaly .....	21
4.5	Computation of Brightness Temperatures .....	22
4.5.1	Antenna pattern matching .....	22
4.5.2	Synthesis of 85 GHz channel data .....	23
4.6	SSM/I Instrument Homogenization.....	24
4.6.1	Earth incidence angle variations.....	24
4.6.2	Intersensor calibration.....	25
4.7	Error Budget Estimates.....	28
4.7.1	Random Error.....	29
4.7.2	Systematic Error.....	30


4.8	Practical Considerations .....	32
4.8.1	Validation .....	32
4.8.2	Quality control .....	33
4.8.3	Outputs (FCDR Product Definition) .....	33
5	Assumptions and Limitations .....	34
6	Implications for Future Mission Specification and Instrument Design.....	34
7	References.....	35
8	Appendix A.....	38
9	Glossary.....	40
IV	SSMIS.....	42

## List of Tables

Table III-1: DMSP SSM/I orbit and sensor specific information. ....	38
Table III-2: Antenna spillover and polarisation leakage factors (Wentz, 1991). ....	38
Table III-3: Calibration across-scan smoothing weights for hot and cold target counts and estimated resulting effective correlation of smoothed calibration coefficients. ....	38
Table III-4: Inter-sensor scaling factors a, calibration offsets b and non-linear coefficients c. ....	39
Table III-5: Summary of estimated systematic error source contributions.....	39

## List of Figures

Figure III-1: Local Equator crossing times of the DMSP platforms. Colours are as follows: F08 orange, F10 blue, F11 black, F13 green, F14 violet, and F15 red. ....	11
Figure III-2: SSM/I scan geometry (from Hollinger et al., 1987). ....	11
Figure III-3: SSM/I FCDR processing flow-chart. ....	13
Figure III-4: Along-scan correction for all SSM/I instruments. These images show the along-scan correction applied to a scene temperature of 200 K. Colours are as follows: cyan 19v, blue 19h, green 22v, orange 37v, red 37h, plum 85v, and violet 85h. ....	18
Figure III-5: Cold count anomaly (left) from SSM/I F13 channel 4 (37 GHz, v) for November 2005. The y-axis represents the fractional orbit angle with ascending equator crossing at 0 and descending equator crossing at 0.5. The x-axis represents the time of the orbit start. A cross-section of the absolute cold counts through the maximum of one intrusion event is shown on the right along the revolution 54926. Positions with identified cold count anomalies are between the vertical lines. The locally fitted reconstruction spline is plotted in cyan.....	20
Figure III-6: Uncorrected slope (left) from channel 2 and mean hot load temperature (right) for one orbit with two sunlight intrusion events. The satellite leaves the Earth's shadow approximately at position 0.28	

	<b>Algorithm Theoretical Basis Document</b> <b>Microwave Imager Radiance FCDR R4</b> <b>SSM/I Brightness Temperatures</b>	Doc. No: SAF/CM/DWD/ATBD/FCDR_SSMI Issue: 2.2 Date: 2022-01-31
---	---	--


and enters the Earth's shadow at position 0.85. Positions with identified warm target anomalies are between the vertical lines. The locally fitted reconstruction splines are plotted in cyan..... 20

Figure III-7: Edge detection results (Laplace operator) for calculated first guess slopes from channel 2 (19 GHz, h) and channel 4 (37 GHz, v) from SSM/I F13 in November 2005. Clearly visible are the detected moonlight intrusions and the positions where the spacecraft leaves and enters the Earth shadow..... 20

Figure III-8: Variation of spacecraft F13 altitude (left) and Earth incidence angle (right) for 2005. The y-axis represents the fractional orbit angle with ascending equator crossing at 0 and descending equator crossing at 0.5. The x-axis represents the time of the orbit start..... 25

Figure III-9: Amplitude [in K] of the climatological diurnal model for December for 37 GHz vertical polarization (left) and 37GHz horizontal polarization (right). ..... 27

Figure III-10: Histograms of brightness temperature differences at 22 GHz between F13 and F11 before inter-calibration (black and grey) and after inter-calibration and EIA normalisation offsets are applied (dark blue, light blue). The brightness temperature differences from the RSS version 6 data record (red and orange) are shown for reference (no EIA offsets applied). ..... 27

	<b>Algorithm Theoretical Basis Document</b> <b>Microwave Imager Radiance FCDR R4</b> <b>SSM/I Brightness Temperatures</b>	Doc. No: SAF/CM/DWD/ATBD/FCDR_SSM Issue: 2.2 Date: 2022-01-31
---	---	---

## I Preface

This document is structured in different logical parts, reflecting the different instrument series used to compile a Fundamental Climate Data Record (FCDR) from conical scanning microwave imagers. After a short introduction, summarizing the current status, the corresponding documents for the parts from the Scanning Multichannel Microwave Radiometer (SMMR) and the Special Sensor Microwave Imager/Sounder (SSMIS) are referenced here. These parts are made available as separate documents. The main part of this document describes the methods to compile the Special Sensor Microwave / Imager (SSM/I) component of the FCDR.


### 1 The EUMETSAT SAF on Climate Monitoring

The importance of climate monitoring with satellites was recognized in 2000 by EUMETSAT Member States when they amended the EUMETSAT Convention to affirm that the EUMETSAT mandate is also to “contribute to the operational monitoring of the climate and the detection of global climatic changes”. Following this, EUMETSAT established within its Satellite Application Facility (SAF) network a dedicated centre, the SAF on Climate Monitoring (CM SAF, <https://www.cmsaf.eu/>).

The consortium of CM SAF currently comprises the Deutscher Wetterdienst (DWD) as host institute, and the partners from the Royal Meteorological Institute of Belgium (RMIB), the Finnish Meteorological Institute (FMI), the Royal Meteorological Institute of the Netherlands (KNMI), the Swedish Meteorological and Hydrological Institute (SMHI), the Meteorological Service of Switzerland (MeteoSwiss), the Meteorological Service of the United Kingdom (UK MetOffice) and the Centre National de la Recherche Scientifique, Laboratoire d’études en Géophysique et Océanographie Spatiales, France (CNRS, LEGOS). Since the beginning in 1999, the EUMETSAT Satellite Application Facility on Climate Monitoring (CM SAF) has developed and will continue to develop capabilities for a sustained generation and provision of Climate Data Records (CDR’s) derived from operational meteorological satellites.

In particular, the generation of long-term data sets is pursued. The ultimate aim is to make the resulting data sets suitable for the analysis of climate variability and potentially the detection of climate trends. CM SAF works in close collaboration with the EUMETSAT Central Facility and liaises with other satellite operators to advance the availability, quality and usability of Fundamental Climate Data Records (FCDRs) as defined by the Global Climate Observing System (GCOS). As a major task, the CM SAF utilizes FCDRs to produce records of Essential Climate Variables (ECVs) as defined by GCOS. Thematically, the focus of CM SAF is on ECVs associated with the global energy and water cycle.

The CM SAF data sets can serve applications related to the new Global Framework of Climate Services initiated by the WMO World Climate Conference-3 in 2009. CM SAF is supporting climate services at national meteorological and hydrological services (NMHSs) with long-term data records but also with data sets produced close to real time that can be used to prepare monthly/annual updates of the state of the climate. Both types of products together allow for a consistent description of mean values, anomalies, variability, and potential trends for the

	<b>Algorithm Theoretical Basis Document</b> <b>Microwave Imager Radiance FCDR R4</b> <b>SSM/I Brightness Temperatures</b>	Doc. No: SAF/CM/DWD/ATBD/FCDR_SSM Issue: 2.2 Date: 2022-01-31
---	---	---

chosen ECVs. CM SAF ECV data sets also serve the improvement of climate models both at global and regional scale.

A catalogue of all available CM SAF products is accessible via the CM SAF webpage, <https://www.cmsaf.eu/>. Here, detailed information about product ordering, add-on tools, sample programs and documentation is provided.

## 2 Introduction


This collection CM SAF Algorithm Theoretical Basis Documents (ATBDs) provides information on the methods and the processing chain implemented for the CM SAF Fundamental Climate Data Record of brightness temperatures (TBs) from the SMMR, the SSM/I and the SSMIS. This fourth release is a continuation of the previous release (available from CM SAF; [http://dx.doi.org/10.5676/EUM\\_SAF\\_CM/FCDR\\_MWI/V003](http://dx.doi.org/10.5676/EUM_SAF_CM/FCDR_MWI/V003)).

Data from the space-borne microwave imagers and sounders such as the Scanning Multichannel Microwave Radiometer (SMMR), Special Sensor Microwave/Imager (SSM/I) and the Special Sensor Microwave Imager/Sounder (SSMIS) are used for a variety of applications, such as analyses of the hydrological cycle (precipitation and evaporation) and related atmospheric and surface parameters, as well as remote sensing of sea ice, soil moisture, and land surface temperatures. Carefully calibrated and homogenised radiance data sets are a fundamental prerequisite for climate analysis, climate monitoring and reanalysis. Several National Meteorological Services and Reanalysis centres assimilate microwave radiances directly and not derived geophysical parameters. Forecast and reanalysis can thus benefit from a Fundamental Climate Data Record (FCDR) of brightness temperatures (Poli et al. 2015). The generation of Thematic Climate Data Records (TCDRs) strongly relies on the availability of FCDRs. Highest possible TCDR quality can be achieved easiest in radiance space, in turn increasing the products value for users.

The predecessors of this data record and the data processor suite have originally been developed at the Max-Planck Institute for Meteorology (MPI-M) and the University of Hamburg (UHH) for the Hamburg Ocean Atmosphere Parameters and Fluxes from Satellite Data (HOAPS, <http://www.hoaps.org/>) climatology. HOAPS is a compilation of climate data records for analysing the water cycle components over the global oceans derived from satellite observation (Andersson et al. 2011). The main satellite instrument employed to retrieve the geophysical parameters is the SSM/I and much work has been invested to process and carefully homogenize all SSM/I instruments onboard the Defence Meteorological Satellite Program (DMSP) platforms F08, F10, F11, F13, F14 and F15 (Andersson et al., 2010).

The HOAPS processing suite has been transferred to CM SAF in a Research to Operations activity in order to provide a sustained processing of the climate data records which is one of the main tasks of CM SAF, but not in the focus of the research group at the MPI-M/ UHH. The operational processing and reprocessing of the FCDRs and TCDRs as well as the provision to the research community is maintained and coordinated by the CM SAF.

The first release of the CM SAF FCDR (Fennig et al. 2013) focussed on the SSM/I series, covering the time period from 1987 to end of 2008. In order to continue the HOAPS TCDRs beyond 2008 it was necessary to extend the underlying FCDR of microwave TBs with the

	<b>Algorithm Theoretical Basis Document</b> <b>Microwave Imager Radiance FCDR R4</b> <b>SSM/I Brightness Temperatures</b>	Doc. No: SAF/CM/DWD/ATBD/FCDR_SSM Issue: 2.2 Date: 2022-01-31
---	---	---

SSMIS sensor family aboard the DMSP platforms F16, F17, and F18, which was accomplished with the second release of the CM SAF FCDR (Fennig et al. 2015). This combined FCDR of SSM/I and SSMIS brightness temperatures provides a consistent FCDR from 1987 to 2013.

Following requests from users of the FCDR, the third release focussed on the extension of the microwave brightness temperature data record to the earlier time period from 1978 to 1987 with observations from the SMMR on-board Nimbus-7. However, this turned out to be a very challenging task, as it has not been possible to get hold of the original raw instrument data records. Although this data record must have eventually been transferred from the Marshall Space Flight Centre (MSFC) to the National Snow & Ice Data Center (NSIDC), it is currently not available from their archives. Instead, the Nimbus-7 SMMR Pathfinder Level 1B Brightness Temperatures data record, available from NSIDC (Njoku, 2003), is used to generate this FCDR.

The third release of the FCDR is described in Fennig et al. (2020) which also includes a decent overview of the applied methodologies.

With the 4<sup>th</sup> release of the Microwave Imager Radiance FCDR, the temporal coverage of the SSMIS has been extended to 31 December 2020 while the SMMR and SSM/I data records remain unchanged. The data records for the SSMIS sensors on-board F16, F17, and F18 have been reprocessed for this fourth FCDR release, implementing significant improvements.

## II SMMR

The algorithms and methods to build the SMMR FCDR component have not been changed compared to the last release and are described in the corresponding ATBD [RD 1].

### III SSM/I

This part of the document focuses on the methods and procedures to process the SSM/I data record.

## 3 Algorithm Overview

### 3.1 The SSM/I Instrument

SSM/I sensors have been carried aboard the DMSP satellite series since 1987. Up to three radiometers have been in orbit simultaneously, as shown in Figure III-1. An extensive description of the instrument and satellite characteristics has been published by Hollinger (1987) and Wentz (1991). Hence, only a short summary of essential information is given here. The DMSP satellites operate in a near-circular, sun-synchronous orbit, with an inclination of  $98.8^\circ$  at an approximate altitude of 860 km. Each day, 14.1 orbits with a period of about 102 minutes are performed. The Earth's surface is sampled with a conical scan at a constant antenna boresight angle of  $45^\circ$  over an angular sector of  $102.4^\circ$  resulting in a 1400 km wide swath (Figure III-2). A nearly complete coverage of the Earth by one SSM/I instrument is achieved within two to three days. Due to the orbit inclination and swath width, the regions poleward of  $87.5^\circ$  are not covered.

To date, six SSM/I instruments have been successfully launched aboard the F08, F10, F11, F13, F14 and F15 spacecrafts. All satellites have a local equator crossing time between 5 and 10 A.M./P.M. for the descending/ascending node. The F08 had a reversed orbit with the ascending node in the morning. Also, the Earth observing angular sector of the scan on this satellite is, differently from the others, centred to the aft of the sub-satellite track.

Most of the DMSP satellites have a stable orbit as shown in Figure III-1. The temporal variation of the equator crossing times is less than three hours for all satellites. At the end of the time period the orbits of F14 and F15 begin to decay noticeably, but are still within 2-3 hours of original time.

The SSM/I is a seven channel total power radiometer measuring emitted microwave radiation at four frequency intervals centred at 19.35, 22.235, 37.0, and 85.5 GHz. All frequencies are sampled at horizontal and vertical polarization, except for the 22.235 GHz channel, which measures only vertically polarized radiation. The channels will be referred to as 19, 22, 37, and 85 GHz hereafter and the corresponding brightness temperatures of each channel and polarization as TB19v/h, TB22v, TB37v/h, and TB85v/h.

The spatial resolution varies from 69 km by 43 km with a sampling frequency of 25 km for the 19 GHz channel to 15 km by 13 km with 12.5 km sampling frequency for the 85 GHz channel. The 85 GHz channels are sampled for each rotation of the instrument (A and B-scans) with a resolution of 128 uniformly spaced pixels, while the remaining channels are sampled every other scan (A-scans) with a resolution of 64 pixels (see Figure III-2). A fixed cold space reflector and a reference black body hot load are used for continuous onboard two point calibration (see section 4.3).

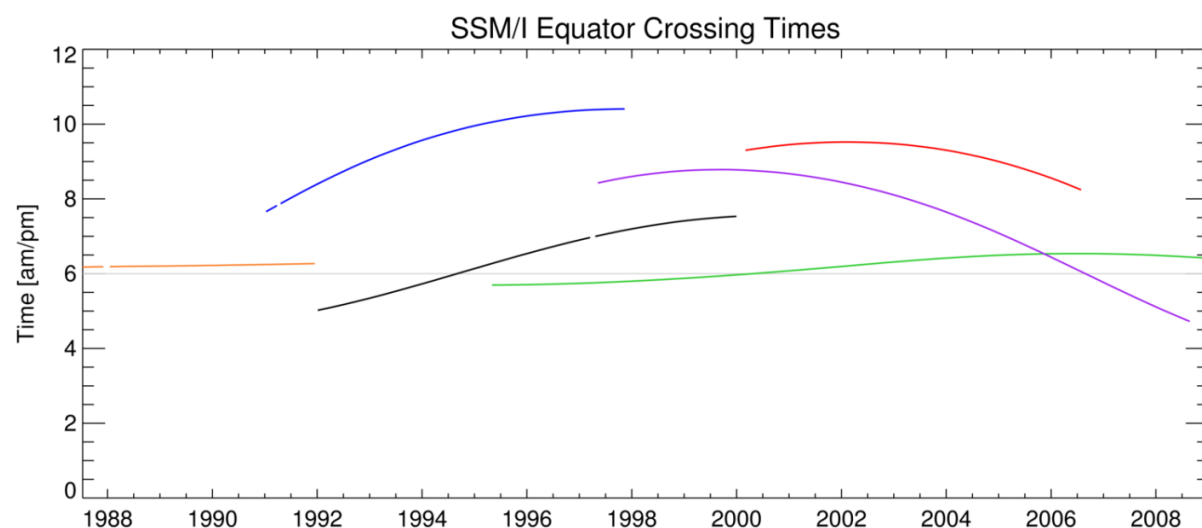


**Figure III-1:** Local Equator crossing times of the DMSP platforms. Colours are as follows: F08 orange, F10 blue, F11 black, F13 green, F14 violet, and F15 red.

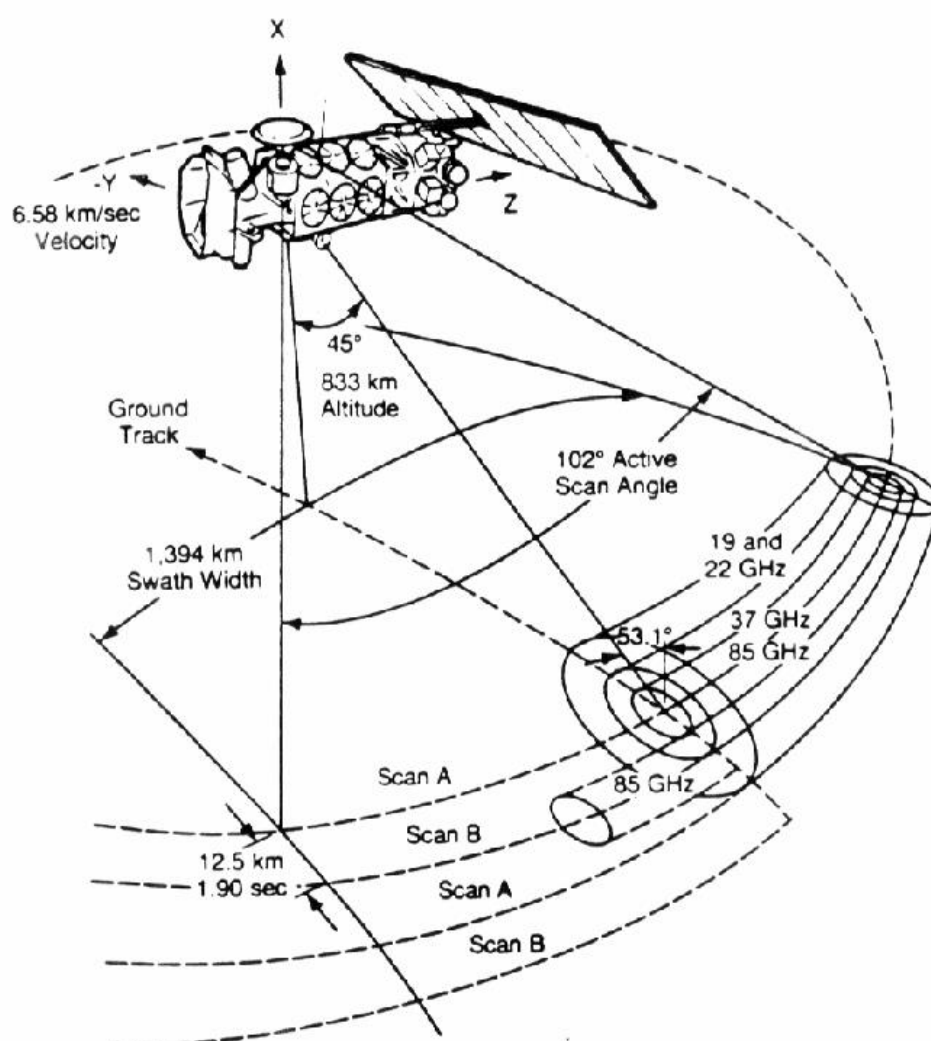


**Figure III-2:** SSM/I scan geometry (from Hollinger et al., 1987).

## 4 Algorithm Description

This section provides information on the processing chain implemented to compile the SSM/I Fundamental Climate Data Records (FCDR).

### 4.1 FCDR data processing

The SSM/I data processing is split into level-1a,b and level-1c processing steps (see Figure III-3). During the level-1a,b processing step, all different raw data records are reformatted into a common data format. Raw data records used as input to compile the FCDR are:

- Antenna Temperatures from Remote Sensing Systems (RSS),
- Temperature Data Records (TDR) from the National Environmental Satellite, Data, and Information System (NESDIS),
- and reformatted NetCDF TDR data files from the National Climate Data Center (NCDC) (Semunegus, 2010).

The combined usage of different data sources is necessary because they cover different time periods and have different coverage due to missing files, checksum errors and corrupt data records.


An analysis of SSM/I data from different sources (Ritchie et al., 1998), including NESDIS TDR and RSS data, showed no systematic differences between these data sets. Moreover, our own analysis showed that apart from the geolocation, which is different in the RSS files (Wentz, 1991), the same information is available in all data files.

To merge the scans from all different sources, unique MD5 hash values are computed from the calibration data. The MD5 algorithm is a cryptographic hash function that takes a block of data and returns a unique fixed size hash value that can be used as a fingerprint to identify the data block. This MD5 hash value is used in the level-1c processing to find identical scan-lines and to correctly merge all available data records to compile the FCDR files. During the first processing step antenna temperatures are reverted to Earth counts as the pre-processed TDR input data can contain erroneous calibration slopes and offsets caused by an averaging of the calibration data without quality control tests (Ritchie et al., 1998).

In the following processing step the spacecraft position and the geolocation is computed (see section 4.2), the water/land surface type is assigned to each FOV (see section 4.2.1), a first raw data calibration is done (ignoring intrusion events) to convert from Earth counts to antenna temperatures (see section 4.3) and the quality control flags are assigned (see section 4.8.2). From these intermediate data files yearly monitoring files are compiled where the calibration and geolocation is sampled at fixed orbit angle positions. These files are analyzed to identify and correct for cold and hot view intrusions (see sections 4.4.2 and 4.4.3). The corrected cold and hot calibration counts are used to derive the final calibration coefficients and to compute antenna temperatures (TAs). An along-scan correction is applied to the TAs (section 4.4.1) to account for a non-uniformity of the measured antenna temperatures along a scan-line.

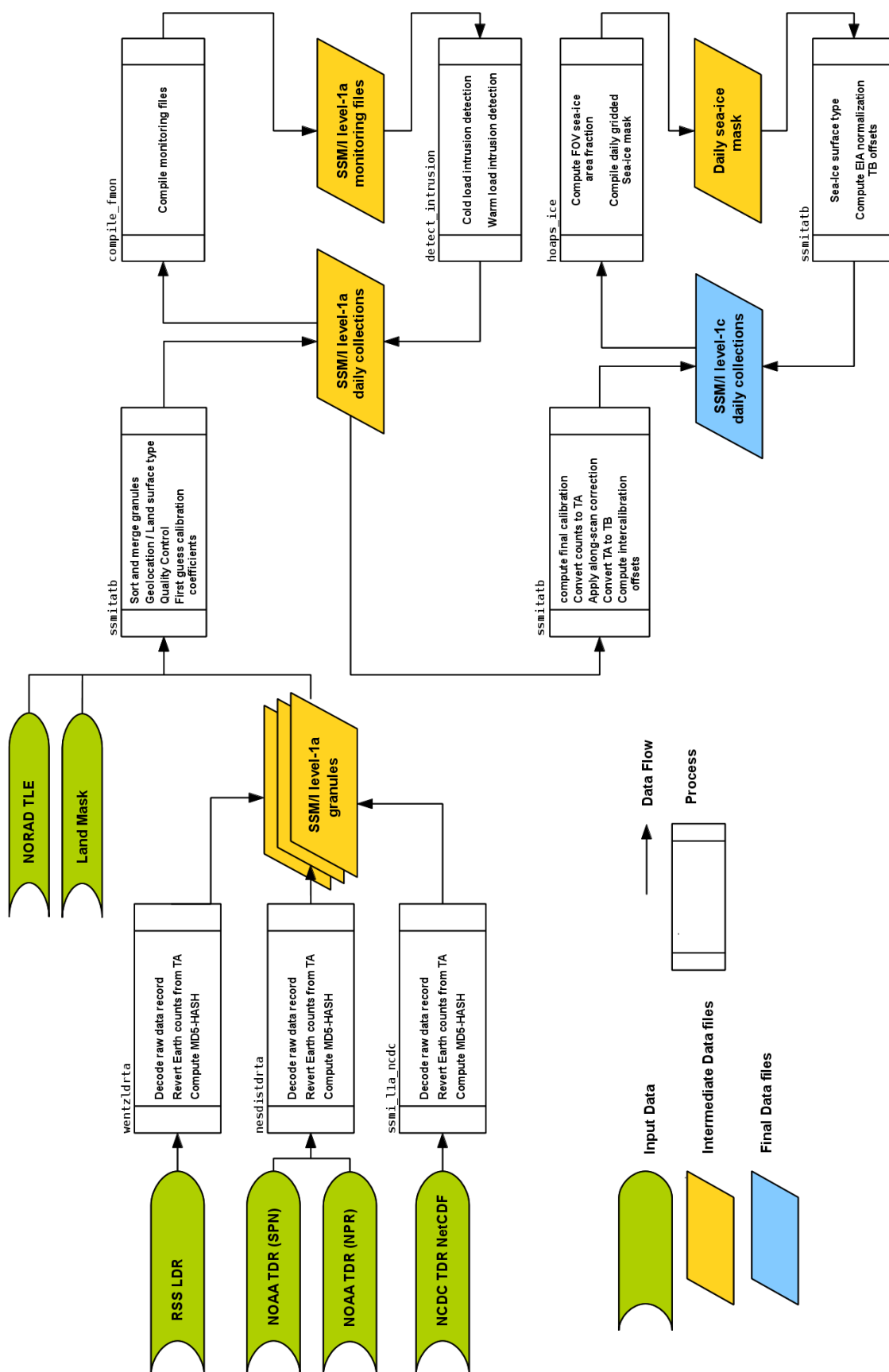


**Figure III-3: SSM/I FCDR processing flow-chart.**

	<b>Algorithm Theoretical Basis Document</b> <b>Microwave Imager Radiance FCDR R4</b> <b>SSM/I Brightness Temperatures</b>	Doc. No: SAF/CM/DWD/ATBD/FCDR_SSM Issue: 2.2 Date: 2022-01-31
---	---	---

The corrected antenna temperatures are then converted to brightness temperatures (see section 4.5) and the inter-sensor calibration offsets (section 4.6.2) are computed. Now the sea-ice concentration is derived for each FOV and daily ice masks are compiled (section 4.2.1). Finally the sea-ice and sea-ice margin surface types are assigned, the Earth incidence angle normalisation offsets are computed for water type FOVs (section 4.6.1) and the high-resolution channels are averaged to provide additional information on the lower resolution (section 4.5.1).

## 4.2 Geolocation

The quality of the SSM/I geolocation has been examined by Poe and Conway (1990) and Colton and Poe (1999). The operational requirement of geolocating SSM/I data is defined by half the 3dB beam diameter of the high-resolution 85 GHz channels, which translates to about 7 km location error requirement. The studies showed that the predicted spacecraft ephemeris in the data records caused an error of up to 15 km. Since July 1989 the processing was changed and the new ephemeris error is typically less than 2-3 km. To reduce the SSM/I geolocation error below the requirement a fixed set of spacecraft attitude corrections were determined. These attitude corrections are found for each instrument (see Table III-1 in Appendix A). Colton and Poe (1999) finally conclude that the RMS of the geolocation error is less than 4 km.

In order to provide a homogeneous product, all geolocation data must be recalculated during the processing. The spacecraft position is predicted with the Simplified General Perturbations model SGP4 (Hoots and Roerich, 1988). This model uses North American Aerospace Defense Command (NORAD) ephemeris sets to predict position and velocity of Earth-orbiting objects. The element sets for the time period up to January 2000 are freely available and used until December 1999. In order to use the SGP4 model throughout the complete time period, the ephemeris data from the raw data records have been used to find the orbit elements in a minimization fitting procedure for all data files after 2000.

This fitted ephemeris data is determined for each day and then smoothed using a moving averaging window of  $\pm 7$  days. A comparable method is used by Wentz (1991) to fit a simple orbit model. The accuracy is usually better than 1 km compared to original data and compared to time periods with available NORAD element sets. The spacecraft position is predicted for all B-scan times and archived in the FCDR data files.

During the geolocation procedure the spacecraft position is linearly interpolated to each pixel time in an Earth-centred inertial (ECI) coordinate frame by applying a rotation matrix. The rotation axis is found as the vector cross product between two spacecraft positions. The magnitude of the vector is linearly interpolated. From this spacecraft position at pixel time the location of the FOV on the Earth surface is found as the intersection of the antenna beam with the Earth surface following the geolocation procedure described in Hollinger (1989) and Wentz (1991).

The spacecraft attitude corrections for pitch and roll are found using a method similar to the approach of Berg et al. (2012), where the roll angle is estimated from the slope of the mean TB along the scan line. Changes in spacecraft roll and pitch have a distinct effect on the vertically polarised TBs: A change in pitch modifies the curvature along the scan and a change in roll results in a gradient along the scan. The method from Berg et al. (2012) has been

modified to fit both angle offsets, roll and pitch, from the TB variation along the scan. Instead of using only vertically polarised channels for the minimization procedure as in the original technique, polarization differences are employed as the horizontally polarised channels are much less affected. This minimizes the influence of cold intrusions at the scan edge (see also section 4.4.1) and all FOV positions, weighted with the position dependent variability, can be used to find mean values for pitch and roll offsets. After applying the correction, the TB variation along the scan appears very similar for all instruments (see Figure III-4). Corrections for yaw and elevation offset are found empirically from a coastline analysis using the high resolution horizontal 85GHz channel. The spacecraft attitude corrections are summarized in Table III-1.

While comparing the new and the original geolocation it was found that both agree usually within  $\pm 2$  km. However, the original data shows a gradual degradation within a few days followed by sudden jumps when the ephemeris was updated again.

Another problem that was identified in the raw data records is an inconsistent handling of leap seconds. During the time period from 1987 to 2008 ten leap seconds are officially inserted. It can take up to 7 days before a leap second is introduced to the SSM/I data files. The time difference itself is not problematic if the observation time and the ephemeris time are updated synchronously but a geolocation error of about 7 km is visible if this is not the case. This has been corrected in the CM SAF FCDR and the observation times are changed in a way that all leap seconds are introduced at the correct times.

#### 4.2.1 Land mask and sea ice detection

Each FOV is characterized with a surface type classification flag using the CF-Metadata convention for flag variables (providing all information via the attributes *flag\_values* and *flag\_meanings*). Possible surface types are: water, land, coast, coast2, sea-ice, and sea-ice margin. The centre latitude and longitude of the FOV is used to assign the surface type. Two surface type variables are included in the FCDR data files: one for the low-resolution channels and one for the high-resolution channels.

The SSM/I specific land-sea mask is derived from the Global Land One-km Base Elevation data base (GLOBE, 1999). This data set is further adjusted to the SSM/I footprint resolutions by first removing small islands and landmasses with a diameter of less than 5 km for the low-resolution channels and 2 km for high-resolution channels, treating these areas as open water. This provides the basic land-sea classification. In a second step the coastal areas are defined by expanding the remaining land areas 50 km (low resolution) or 15 km (high resolution) into the sea. The surface type coast2 is assigned to regions that are defined as open water in the high resolution land mask, but are more than 50 km away from the nearest water area in the low resolution land mask.

To account for the varying sea ice margins, a daily sea-ice mask is compiled from the SSM/I brightness temperatures. These maps are created in two steps. First, the total sea ice covered fraction within a single SSM/I FOV is computed using the NASA Team sea ice algorithm of Swift (1985). The resulting sea ice observations from all available SSM/I instruments are then gridded to common daily mean fields on a regular  $0.5^\circ \times 0.5^\circ$  grid. In order to distinguish between short-lived strong rain events and persisting sea ice, which are characterized by similar TB signatures, only grid boxes with an average sea ice fraction above 15% for at least

5 consecutive days are flagged as ice covered. This filter thus removes all ice events lasting less than 5 days from the first guess ice mask. Daily sea ice maps are then derived from this reduced data set by re-expanding the reliably identified sea ice areas in time and space and filling remaining data gaps by spatial and temporal interpolation. Finally, the resulting sea ice margin is extended 50 km into the ocean which leads to the sea-ice and sea-ice margin surface types.

### 4.3 SSM/I calibration

The basic underlying assumption for the SSM/I calibration is a linear relation of the radiometer output voltage (measured in counts) to the radiometric input at the mixer, neglecting non-linear effects in the square-law detector. In this case two reference targets with known temperatures and corresponding radiometer measurements are sufficient for an absolute linear two-point calibration.

The warm calibration target of the SSM/I is an internal black-body radiator with three embedded thermistors, constantly measuring its temperature. The cold reference target is a mirror pointing to the cold space, with an assumed constant temperature at 2.7 K. The radiometer views the internal warm and cold calibration targets once during a scan rotation. For all instrument channels five radiometric readings are taken for both calibration targets during an A-scan and five additional measurements are taken for the 85 GHz channels during a B-scan. The three embedded thermistor readings are available once per scan pair. The calibration slopes  $S$  in  $K/count$  and offsets  $O$  in  $K$  for each channel are calculated following Hollinger (1987) as follows:

$$S = \frac{\langle T^H \rangle - T^C}{\langle C^H \rangle - \langle C^C \rangle}$$

$$O = \frac{T^C \cdot \langle C^H \rangle - \langle T^H \rangle \cdot \langle C^C \rangle}{\langle C^H \rangle - \langle C^C \rangle},$$

**Equation III-1**

where

$$\begin{aligned} \langle C^H \rangle &= \text{Smoothed mean hot counts} \\ \langle C^C \rangle &= \text{Smoothed mean cold counts} \\ \langle T^H \rangle &= \text{Corrected smoothed mean hot load temperature} \\ T^C &= \text{Cold target temperature (= 2.7K).} \end{aligned}$$

The smoothed mean scan-line values for the cold counts, the hot counts, and the warm target temperature are derived by first averaging all available measurements for both the A and B scan that pass the quality control (see section 4.8.2):

$$\overline{C^H} = \frac{1}{5} \cdot \sum_{i=1}^5 C_i^H \quad \overline{C^C} = \frac{1}{5} \cdot \sum_{i=1}^5 C_i^C \quad \overline{T^{HL}} = \frac{1}{3} \cdot \sum_{i=1}^3 T_i^{HL} \quad \text{Equation III-2}$$

where  $C_i^H, C_i^C, T_i^{HL}$  are the samples of the hot target, the cold target, and the hot load target thermistors respectively. In order to further reduce the noise in the calibration input values, an additional Gaussian smoothing of these scan-line mean values, denoted with the  $\langle \rangle$  operator is applied:

$$\begin{aligned} \langle \overline{C^H} \rangle &= \sum_{i=s-5}^{s+5} w_i \cdot \overline{C^H}_i \bigg/ \sum_{i=-5}^5 w_i \\ \langle \overline{C^C} \rangle &= \sum_{i=s-5}^{s+5} w_i \cdot \overline{C^C}_i \bigg/ \sum_{i=-5}^5 w_i \\ \langle \overline{T^{HL}} \rangle &= \sum_{i=s-5}^{s+5} w_i \cdot \overline{T^{HL}}_i \bigg/ \sum_{i=-5}^5 w_i \quad , \end{aligned} \quad \text{Equation III-3}$$

where  $w_i$  are the Gaussian across-scan weights. The moving averaging kernel spans the five preceding and five following mean scan-line values. Thus the smoothing process introduces an artificial error correlation in the smoothed calibration coefficients. However, as the variance of the calculated brightness temperatures is dominated by the variance in the independently measured Earths counts (98%, see section 4.7.1), the impact of the error correlation in the smoothed calibration coefficients on the final brightness temperatures can be neglected. The applied Gaussian weights and estimated effective correlations for the smoothed calibration coefficients resulting from the averaging procedure are listed in Table III-3 in Appendix A.

The mean temperature of the warm target  $\overline{T^{HL}}$  is corrected using the temperature of the forward radiator plate  $T^P$  to account for radiative coupling between the hot-load and the top plate of the rotating drum assembly which faces the hot-load when not being viewed:

$$\langle T^H \rangle = \varepsilon \cdot \langle \overline{T^{HL}} \rangle + (1 - \varepsilon) \cdot \langle T^P \rangle \quad \text{Equation III-4}$$

The value for  $\varepsilon$  is empirically determined from thermal-vacuum calibration (Hollinger, 1987). The original value of 0.99 has been changed to sensor specific values determined during the inter-sensor calibration procedure (see Table III-1 in Appendix A)

Slopes and offsets are archived in the FCDR data files for reference. The antenna temperatures are then calculated from the Earth counts  $C^E$  for each FOV as follows:

$$T_A = S \cdot C^E + O \quad \text{Equation III-5}$$

## 4.4 Applied corrections

### 4.4.1 Along-scan correction

One of the first detected SSM/I calibration problems was the non-uniformity of the measured antenna temperatures along a scan-line (Wentz, 1991; Colton and Poe, 1999). A rapid fall-off at the end of the Earth scan of nearly 1.5 to 2 K was found in all SSM/I channels. This

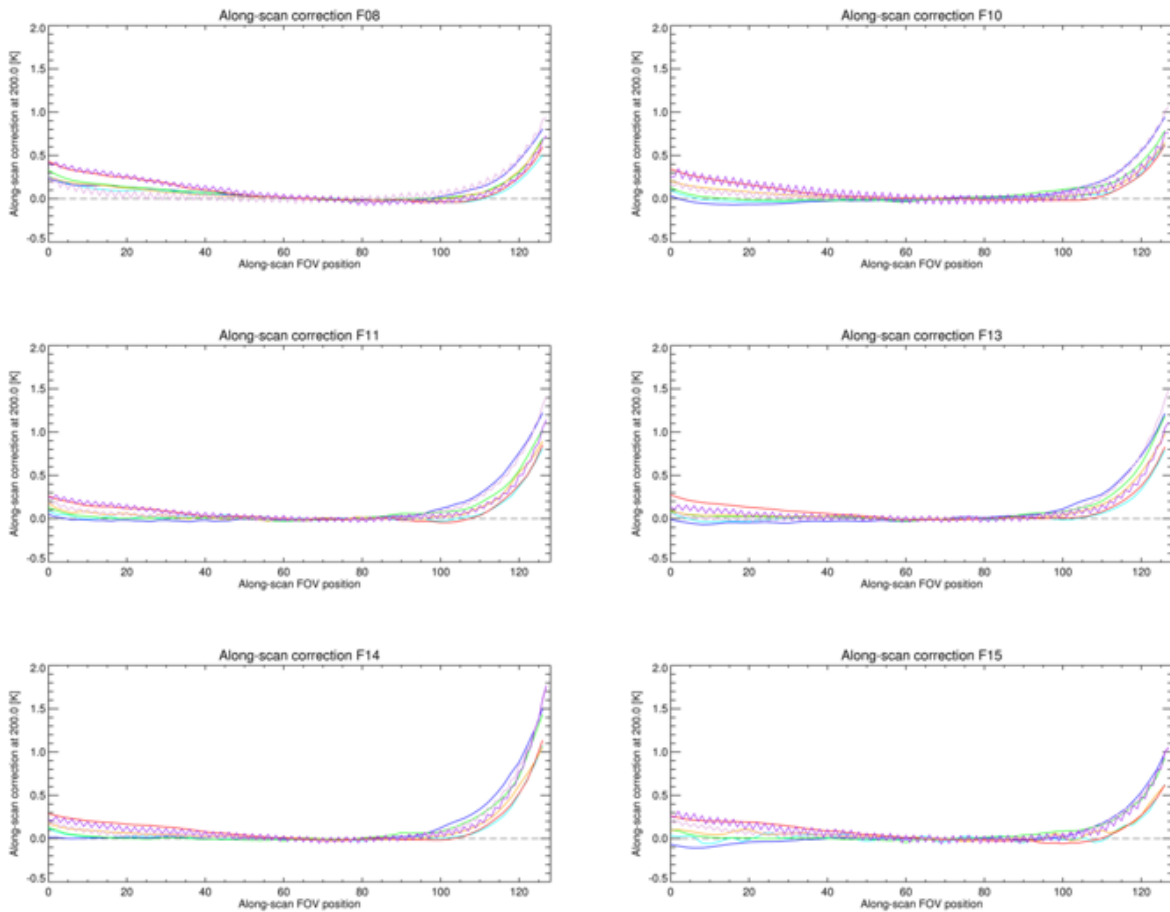


**Figure III-4:** Along-scan correction for all SSM/I instruments. These images show the along-scan correction applied to a scene temperature of 200 K. Colours are as follows: cyan 19v, blue 19h, green 22v, orange 37v, red 37h, plum 85v, and violet 85h.

systematic problem is caused by an intrusion of cosmic background energy by the glare Suppression System-B (Colton and Poe, 1999) into the antenna feedhorn reducing the upwelling scene temperature.

This effect of FOV intrusion can be treated as a beam-position energy loss which can be corrected by multiplying the antenna temperature  $T_A$  with a scan position depended factor. This factor is derived in a two step procedure. First,  $T_A$  values for each satellite and channel with surface type sea between 50°S and 50°N are EIA normalized and averaged into FOV-position bins for a least one year. Then the factor at each FOV position is computed as the ratio of the position averaged value to the total average along the unaffected FOVs at the scan line centre (50-90). The along-scan correction factors, multiplied with a scene temperature of 200 K, for all instruments are shown in Figure III-4.

#### 4.4.2 Cold view intrusions

The SSM/I calibration procedure assumes that the cold reference target is at the background cosmic temperature of 2.7 K. However, due to the instrument design it is possible, depending on the orbit parameters, that the moon is visible in the cold view. This leads to a short term

increase in the measured cold target radiation counts. This increase depends on the beamwidth of the channels as the fraction of the moon in the FOV compared to the cosmic background is larger for smaller beamwidths. These events happen usually twice per month, depending on the orbit configuration. An example is shown in Figure III-5. This plot shows the anomaly (high-pass filtered) of the 37v GHz cold counts from SSM/I on F13 for November 2005 (on the left) and the absolute cold counts for one orbit at the maximum of the moonlight intrusion event (on the right).

As these events only affect the cold reference target, the impact on the calibrated antenna temperatures are larger for lower scene temperatures. The best way to correct this effect is to apply a band-pass filter to remove the additional signal induced from the moonlight. Under normal conditions the variation of the cold counts is periodic and changes very little from orbit to orbit. This allows to easily detect the anomalies as shown in Figure III-5.

A procedure has been developed which automatically detects the moonlight intrusion events using a Laplace filter as an edge detection algorithm. The Laplace operator computes the second derivatives of an image, measuring the rate at which the first derivatives change. This determines if a change in adjacent pixel values is from an edge or continuous progression. In order to use standard image filtering techniques to detect the intrusion events, yearly monitoring files are compiled where the calibration data is sampled at fixed orbit angle positions. The discrete Laplace operator is then defined as:

$$\Delta_{i,j}^c = 2 \cdot \hat{C}_{i,j}^c - \hat{C}_{i-k/2}^c - \hat{C}_{i+k/2}^c \quad \text{Equation III-6}$$

with  $i$  and  $j$  are the along-orbit and across-orbit image indices respectively,  $k$  is the kernel size, and  $\hat{C}^c$  are the sampled cold counts. This image is then smoothed and periods with moonlight intrusion are detected where the derived Laplacian is significantly larger than one standard deviation of the complete field. These periods are regarded as missing data and reconstructed along the orbit using a Spline interpolation procedure from the neighbouring smoothed valid values. The difference between the original and the reconstructed values is smoothed and removed from the original values. Thus this procedure is similar to a local band-pass filter but can also deal with undefined data. Affected scans are marked during the final data processing using the processing control flag.

#### 4.4.3 Hot load intrusions

Another problem detected in the SSM/I calibration data is a direct sunlight intrusion into the warm reference target. This happens during certain orbit constellations when the satellite is leaving and entering the Earth shadow. A similar problem has also been reported for the SSMIS instrument (Kunkee and Poe, 2008).

The direct sunlight causes a fast instant response in the measured radiation from the black-body as the radiation is emitted and reflected from its surface. As the three hot-load temperature sensors are embedded into the black-body they do not measure the surface temperature of the calibration target but more a core temperature. This delayed response of the temperature sensors leads to abrupt heating and cooling events.

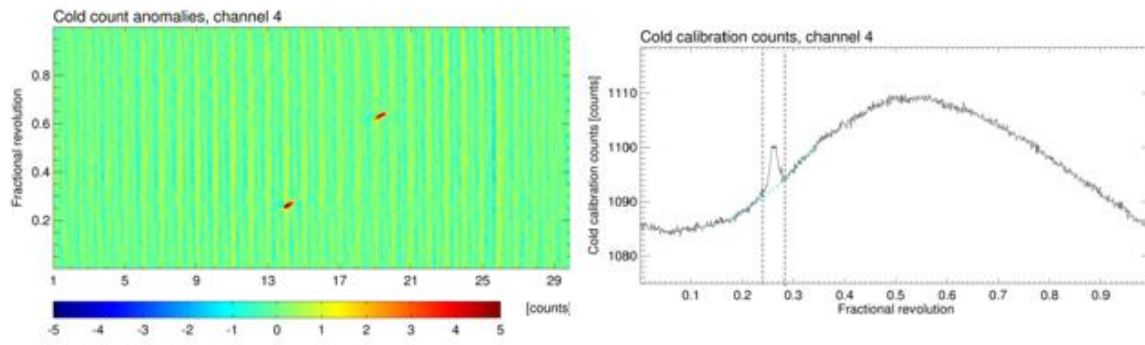


**Figure III-5:** Cold count anomaly (left) from SSM/I F13 channel 4 (37 GHz, v) for November 2005. The y-axis represents the fractional orbit angle with ascending equator crossing at 0 and descending equator crossing at 0.5. The x-axis represents the time of the orbit start. A cross-section of the absolute cold counts through the maximum of one intrusion event is shown on the right along the revolution 54926. Positions with identified cold count anomalies are between the vertical lines. The locally fitted reconstruction spline is plotted in cyan.

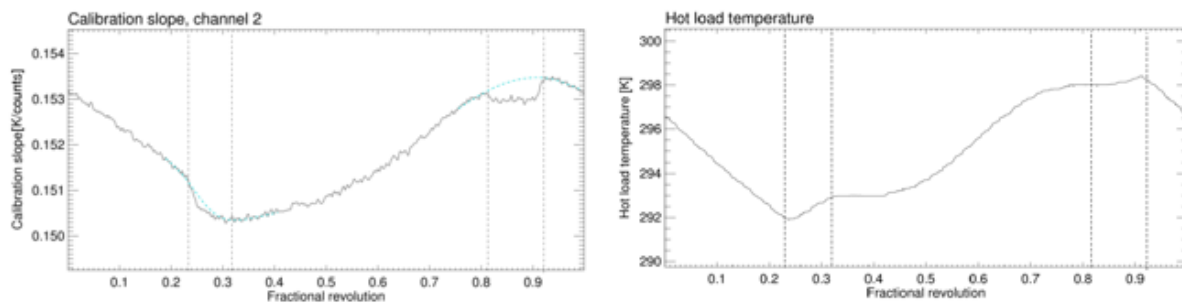


**Figure III-6:** Uncorrected slope (left) from channel 2 and mean hot load temperature (right) for one orbit with two sunlight intrusion events. The satellite leaves the Earth's shadow approximately at position 0.28 and enters the Earth's shadow at position 0.85. Positions with identified warm target anomalies are between the vertical lines. The locally fitted reconstruction splines are plotted in cyan.

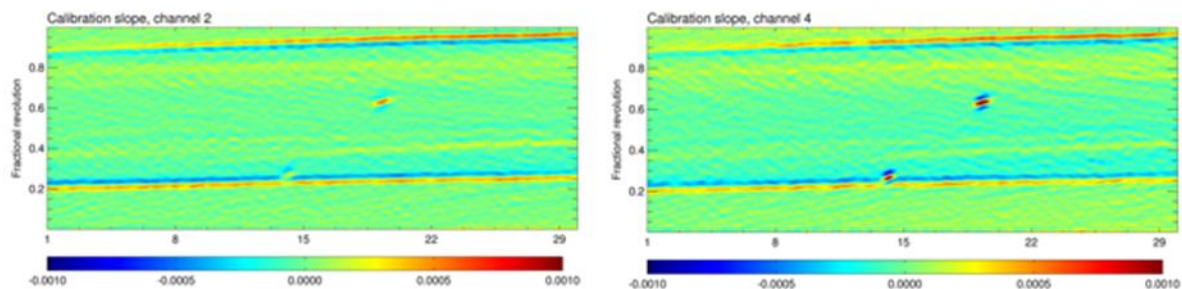


**Figure III-7:** Edge detection results (Laplace operator) for calculated first guess slopes from channel 2 (19 GHz, h) and channel 4 (37 GHz, v) from SSM/I F13 in November 2005. Clearly visible are the detected moonlight intrusions and the positions where the spacecraft leaves and enters the Earth shadow.

The sunlight intrusion can be detected by analyzing the computed calibration slopes. An example is presented in Figure III-6. When the sunlight falls directly onto the hot-load, the measured radiation increases but the temperature gradient along the orbit remains unchanged due to the slower response time of the temperature sensors. This leads to a sudden decrease in the computed calibration slopes (around positions 0.23 and 0.81). If the satellite leaves the Earth's shadow, the whole instrument warms up, and the hot-load temperature starts to increase until core and surface temperature are balanced again (around position 0.32). However, if the satellite enters the Earth's shadow the intrusion effect is more pronounced. As long as the sunlight falls on the hot-load, a negative anomaly can be observed in the calibration slopes. When the sunlight vanishes (around position 0.9) a sharp increase is visible in the slope when hot-load target temperature and measured radiation are balanced again.

This sunlight effect depends on the channel due to the emission characteristics and is strongest for the lower frequencies. The procedure to correct for this intrusion is similar to the correction for the moonlight intrusions (see section 4.4.2), but in the sunlight case the slopes must be corrected as temperature and hot count measurements are both affected. All significant sunlight intrusion events are detected using the edge-detection algorithm applied on the slope anomalies using a discrete Laplace operator applied on the sampled calibration slopes  $\hat{S}$ :

$$\Delta_{i,j}^S = 2 \cdot \hat{S}_{i,j} - \hat{S}_{i-k/2} - \hat{S}_{i+k/2} \quad \text{Equation III-7}$$

This image is then smoothed and periods with sunlight intrusion are detected where the derived Laplacian is significantly larger than one standard deviation of the complete field. These periods are treated as undefined and the missing values are reconstructed from a spline interpolation using the neighbouring smoothed valid slope values (see Figure III-6). The difference between the original and reconstructed values is smoothed and removed from the original values. Thus this procedure is similar to a local band-pass filter but can deal with undefined data. The slope anomalies are then converted (inverted equation III-1) to an anomaly in the hot load counts assuming the temperature readings are correct. Affected scans are marked during the final data processing using the processing control flag.

An example for the edge detection algorithm (Laplace operator) is shown in Figure III-7 for two channels on SSM/I F13 for November 2005. Clearly visible are the two moonlight intrusion events (compare with Figure III-5) and the positions where the spacecraft enters and leaves the Earth shadow with corresponding sunlight intrusion events leading to a sudden decrease or increase in the calibration slope.

#### 4.4.4 F10 Digital Count Anomaly

An anomaly affecting the digital count values of the SSM/I aboard F10 has been identified. The numerical values 2048 and 2049 are missing in the data stream resulting in a jump from 2047 to 2050. This problem occurs when the calibrations counts are larger than 2048, while the Earth counts are below 2048 and leads to a scene dependent bias up to 0.3-0.5 K for all channels. However, the horizontally polarized 85 GHz channel Earth counts are larger than 2048 from about April to October but lower for the rest of the year. This leads to artificial seasonal cycle in the derived  $T_A$ s with an amplitude in the order of 0.5 K. This issue has been

corrected by subtracting 2 counts from all values larger than 2047 before computing the calibration slopes and offsets.

## 4.5 Computation of Brightness Temperatures

The antenna temperature is a direct measure of the radiation entering the antenna feedhorn. It may be expressed in terms of an integral of the scene brightness temperature distribution incident on the antenna reflector and the effective co- and cross-polarized far-field antenna power patterns. To obtain an estimate of brightness temperature  $T_B$  from  $T_A$  it is necessary to apply an Antenna Pattern Correction (APC) to correct for cross-polarization leakage  $\chi_{v,h}$  and feedhorn spillover loss  $\delta$  (Hollinger, 1987). The integration over the antenna FOV can be approximated by (Wentz, 1991):

$$T_{Av} = (1 - \delta) \cdot \frac{T_{Bv} + \chi_v \cdot T_{Bh}}{1 + \chi_v} + \delta \cdot T^C \quad \text{Equation III-8}$$

$$T_{Ah} = (1 - \delta) \cdot \frac{T_{Bh} + \chi_h \cdot T_{Bv}}{1 + \chi_h} + \delta \cdot T^C$$

The equation is inverted to compute the scene brightness temperatures from the measured antenna temperatures:

$$T_{Bv} = \frac{1 + \chi_v}{(1 - \delta) \cdot (1 - \chi_v \chi_h)} \cdot T_{Av} - \frac{\chi_v \cdot (1 + \chi_h)}{(1 - \delta) \cdot (1 - \chi_v \chi_h)} \cdot T_{Ah} - \frac{\delta}{1 - \delta} \cdot T^C \quad \text{Equation III-9}$$

$$T_{Bh} = \frac{1 + \chi_h}{(1 - \delta) \cdot (1 - \chi_v \chi_h)} \cdot T_{Ah} - \frac{\chi_h \cdot (1 + \chi_v)}{(1 - \delta) \cdot (1 - \chi_v \chi_h)} \cdot T_{Av} - \frac{\delta}{1 - \delta} \cdot T^C$$

For the computation, a fixed set of APCs is used, taken from Wentz (1991) instead of sensor specific values (see Table III-2 in Appendix A). Colton and Poe (1999) compared the final differences between TBs computed with sensor specific APCs and the uncorrected TAs. They found that many channels showed significantly larger offsets after applying the sensor specific APCs and concluded it would be best to use a fixed set of APCs for all sensors for a greater consistence across the sensors.

The final brightness temperatures can be reverted to the original antenna temperatures using the equations above and the APCs listed in Table III-2. Thus, it is possible to apply a different set of APCs. Moreover, it is also possible to reconstruct the corrected Earth counts from the antenna temperatures using the archived calibration slopes and offsets.

### 4.5.1 Antenna pattern matching

For the application of geophysical retrieval algorithms it is important that about the same area of the Earth surface is seen by all channels. Due to the higher frequency, a single field of view (FOV) at 85 GHz covers only about 20% of the area sampled at 37 GHz. The 85 GHz channels are sampled twice as often in along and across track direction compared to all other SSM/I channels (see section 3.1). In order to get a comparable coverage with the 85 GHz channels,

nine neighbouring pixels of the A- and B-Scans are averaged down to the resolution of the corresponding 37 GHz pixel. The high resolution 85 GHz brightness temperatures are averaged with their Gaussian weighted distance  $w$  from the centre FOV analogue to the 37 GHz main antenna pattern:

$$T'_B(s, c) = \sum_{i=hs-1}^{hs+1} \sum_{j=hc-1}^{hc+1} w(i - hs, j - hc, c) T_B(i, j) \bigg/ \sum_{i=hs-1}^{hs+1} \sum_{j=hc-1}^{hc+1} w(i - hs, j - hc, c) \quad \text{Equation III-10}$$

where  $hs = s \cdot 2$ ,  
 $hc = c \cdot 2$

are the high resolution along-track and across-track indices respectively and  $s$  and  $c$  are the corresponding low resolution indices. The Gaussian weights for the surrounding 8 pixels depend on the relative position of the centre pixel along the scan line  $c$  due to the geometric of the conical scanning system. A fixed array of pre-calculated averaging weights (64x3x3) is used during the data processing.

The 85 GHz channel brightness temperatures in the FCDR data files are thus available in the original high resolution and sampling (128 pixel, A- and B-scan) and additionally averaged to the lower resolution and sampling of the other channels (64 pixel, A-scan).

FOV Differences between the lower resolution channels at 19, 22, and 37 GHz are not accounted for. The relative coverage of the main antenna pattern beams compared to the 19 GHz channel are about 40% and 80% for the 37 GHz and 22 GHz channel respectively. However, due to the large footprint size compared to the sampling distance the effective FOV of the averaged TBs would be significantly larger than the instantaneous 19 GHz FOV. This could lead to unwanted contaminations in the averaged brightness temperatures especially near coastlines.

#### 4.5.2 Synthesis of 85 GHz channel data

Due to thermal problems, the SSM/I on the DMSP F08 had to be switched off in December 1987. When the radiometer was reactivated, the 85 GHz vertical polarization channel exhibited significantly increased noise levels. Later, similar problems occurred with the 85 GHz horizontal polarization channel (Hollinger, 1990; Wentz, 1992). Therefore, the 85 GHz channels of the SSM/I on DMSP F08 are regarded as defective from April 1988 until the end of the lifetime of the radiometer.

This failure affects all geophysical retrievals using the 85 GHz channels, for example the HOAPS precipitation retrieval (Andersson et al., 2010). A computationally efficient way of handling this problem is to synthesize approximate values of the missing 85 GHz information from the remaining channels. The synthesis is based on a neural network approach, which is used to estimate TB 85v/h of the 9-pixel averaged 85 GHz FOV from the other SSM/I channels (TB 19v/h, TB 22v, and TB 37v/h). The training data set for the neural network was compiled from randomly selected brightness temperatures of SSM/I radiometers on board DMSP F11, F13, and F14 from 1998. More details on the 85 GHz synthesis algorithm are given in Andersson et al. (2010).

The synthesis allows the application of the same retrieval algorithms for all parameters throughout all analysis steps without individual replacement algorithms for each affected parameter. It has, however, to be kept in mind that such a procedure cannot fully reconstruct the specific 85 GHz information but is a computationally convenient way of handling the missing data by a plausible replacement. Moreover, this method is only valid over open water. Over land surfaces this general approach is not applicable due to the strongly varying surface emissivity.

From April 1988 onwards the low-resolution 85 GHz channel information in the FCDR files of the F08 is replaced by the synthesized brightness temperatures for all FOVs classified as open water. All remaining low-resolution FOVs (land, sea-ice, and coastal areas) are set to undefined. The high-resolution 85 GHz brightness temperatures remain unchanged at their original value. The modified scans are marked using a processing control flag. Thus each user can decide to use the original TB 85v, h or the synthesized values for the time period when the 85 GHz channels start to degrade. The 85v GHz finally failed on 30 January 1989 and the 85h GHz channel on 14 February 1991. However, both polarizations are needed to correctly account for the cross-polarization leakage when converting antenna temperatures to brightness temperatures (see section 4.5), which means that TB 85h is only available if TB 85v is available.

## 4.6 SSM/I Instrument Homogenization

### 4.6.1 Earth incidence angle variations

The SSM/I scanning system is designed to observe the Earth's surface under a nominal constant Earth incidence angle (EIA) of  $53^\circ$ . A deviation of one degree from the nominal incidence angle causes brightness temperature changes of up to 2 K depending on surface and atmospheric conditions. Errors in the geophysical parameters can be in the order of 5% to 10% if the variation in the incidence angle is not taken into account (Furhop and Simmer, 1997).

The incidence angle varies mainly due to changes in the altitude of the spacecraft which is caused by the eccentricity of the orbit and the oblateness of the Earth. The EIA can also vary across the scan by approximately  $0.1^\circ$ . Figure III-8 shows the variation of the spacecraft altitude and the EIA for the F13 satellite for a complete year. The altitude varies along the orbit between 840 to 880 km corresponding to a variation of about  $0.3^\circ$  in EIA. Also a seasonal variation is visible with a period of about 122 days. This periodic change is caused by the precession of the argument of perigee due to the Earth's oblateness.

The varying EIA must be taken into account either explicitly by the radiative transfer model or by normalizing the brightness temperatures to a nominal EIA value. This is not only the case when geophysical parameters are derived but also important during the inter-sensor calibration procedure (see section 4.6.2) as two sensors observe the Earth surface under different EIAs. It should also be noted that the altitude differences between the polar regions can be large (up to 30 km in this example) and this effect should be taken into account when simultaneous nadir overpasses are to be used for inter-sensor calibration.

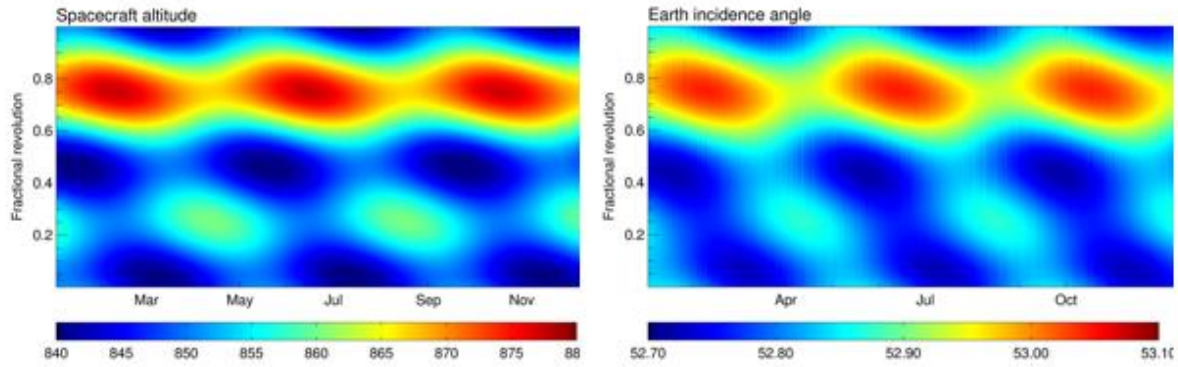


**Figure III-8:** Variation of spacecraft F13 altitude (left) and Earth incidence angle (right) for 2005. The y-axis represents the fractional orbit angle with ascending equator crossing at 0 and descending equator crossing at 0.5. The x-axis represents the time of the orbit start.

Due to the HOAPS heritage of the SSM/I processing software, a normalization of the brightness temperatures has been the default. However, as more advanced techniques, such as 1D or 4D variational analysis, are becoming more widely used, where the radiative transfer model can explicitly account for the varying EIA, this is now considered to be optional. The normalisation to a constant EIA is therefore available as an additional TB offset variable which can be added to the inter-calibrated TBs. The offsets are computed using the method described by Furhop and Simmer (1997) for water type FOVs only. This method uses the measured TBs to estimate the change of the brightness temperature with respect to the EIA (sl):

$$sl = \frac{\delta T_B}{\delta \theta} . \quad \text{Equation III-11}$$

The TBs are then normalized in an iterative procedure:

$$\begin{aligned} sl &= a_0 + \sum_j a_j \cdot T_B(\theta = 53^\circ) \\ T_B(\theta) &= T_B(\theta = 53^\circ) + sl \cdot \Delta \theta \end{aligned} \quad \text{Equation III-12}$$

where  $a_i$  are the regression coefficients of the Furhop and Simmer model. As the slope  $sl$  depends on the atmospheric and surface conditions this procedure is only applicable over ocean because the regression coefficients were determined for this surface type. The final normalization offset  $\Delta T_{EIA}$  is then defined as:

$$\Delta T_{EIA} = T_B(\theta = 53^\circ) - T_B(\theta) \quad \text{Equation III-13}$$

#### 4.6.2 Intersensor calibration

In order to ensure a homogeneous time series of the successive SSM/Is, the slightly varying individual instrument characteristics have to be corrected by an intersensor calibration of the radiometers. The calibration procedure is based on the SSM/I on DMSP F11 which is selected as the reference for a relative intersensor calibration. In tests with different wind speed algorithms against collocated in-situ buoy data this radiometer exhibits a reliable long-term

stability. Furthermore it has a temporal overlap with most of the other radiometers which allows a direct inter-calibration (see Figure III-1). The SSM/Is aboard F08 and F15, which do not have a temporal overlap with F11, are calibrated to the corrected F10 and F13 radiometers used as the transfer standard, respectively. The inter-calibration method used is an updated version of the homogenization scheme described in Andersson et al. (2010). As the largest expected systematic uncertainties (non-linearity and APC coefficients, see section 4.7.2) depend on the scene temperature, an intercalibration model is fitted to correct for observed inter-sensor differences composed of a linear scene dependent term and a non-linear term which depends on the difference of the scene temperature from the calibration targets:

$$T'_B = T_B + c \cdot (T_B - \langle T^H \rangle) \cdot (T_B - T^C) \quad \text{Equation III-14}$$

$$T''_B = a \cdot T'_B + b \quad .$$

The inter-sensor calibration slopes  $a$  and offsets  $b$  and the non-linear term  $c$  are determined by fitting the inter-calibration model (equation III-14) using match-up data sets of the radiometers compiled from the final brightness temperatures on the lower SSM/I resolution. This includes all corrections plus the zenith angle normalization offsets are applied to derive the inter-sensor calibration coefficients at a fixed Earth incidence angle. The match-up data sets are constructed from oceanic, sea-ice and cold scenes over land of each channel binned into a daily global  $1^\circ$  by  $1^\circ$  grid, separately for ascending and descending orbits.

As the equator crossing times vary slightly it allows the observation of the same location on the Earth surface from different radiometers within a time window of less than 3 hours (see Figure III-1). However, the slow change in equator overpass time must be taken into account as it changes the mean morning and evening TB offsets. The major contributor to the diurnal cycle over ocean is cloud liquid water (LWP) due to clouds drying off in the morning and moistening in the evening. This effect has been studied by O'Dell et al. (2008) using microwave satellite data. They found that a sinusoidal model can be used to capture the diurnal cycle of LWP over the majority of the global ocean. This method has been adapted here to fit a simple climatological diurnal cycle model for the SSM/I brightness temperatures  $T_B$  for each channel, grid box, and month:

$$T_B(y_i, t_i) = \bar{T}_B + A \cdot \cos\left(\frac{t_i - T}{12} \cdot \pi\right), \quad \text{Equation III-15}$$

where  $y_i$  is the year corresponding to the  $i$ th observation and  $t_i$  is the local time in hours. The minimization procedure finds the climatological mean brightness temperature  $\bar{T}_B$ , the amplitude  $A$  and the phase  $T$  using all available monthly mean SSM/I data. This diurnal cycle model is then used to normalize the gridded  $T_B$  values by removing the climatological diurnal variation. Figure III-9 shows examples of the fitted amplitudes for two channels (TB37v and TB37h). The strongest diurnal cycle can be observed off the west coast of South America. Generally the amplitudes increase with increasing frequency and are larger for horizontally polarized channels. The local time of the maximum value is typically around 4 AM to 6 AM.

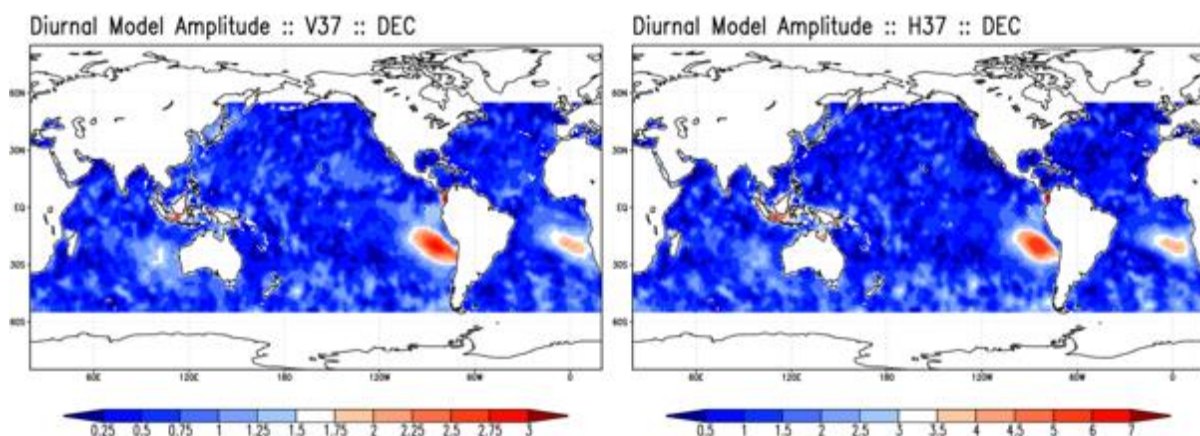


**Figure III-9:** Amplitude [in K] of the climatological diurnal model for December for 37 GHz vertical polarization (left) and 37GHz horizontal polarization (right).

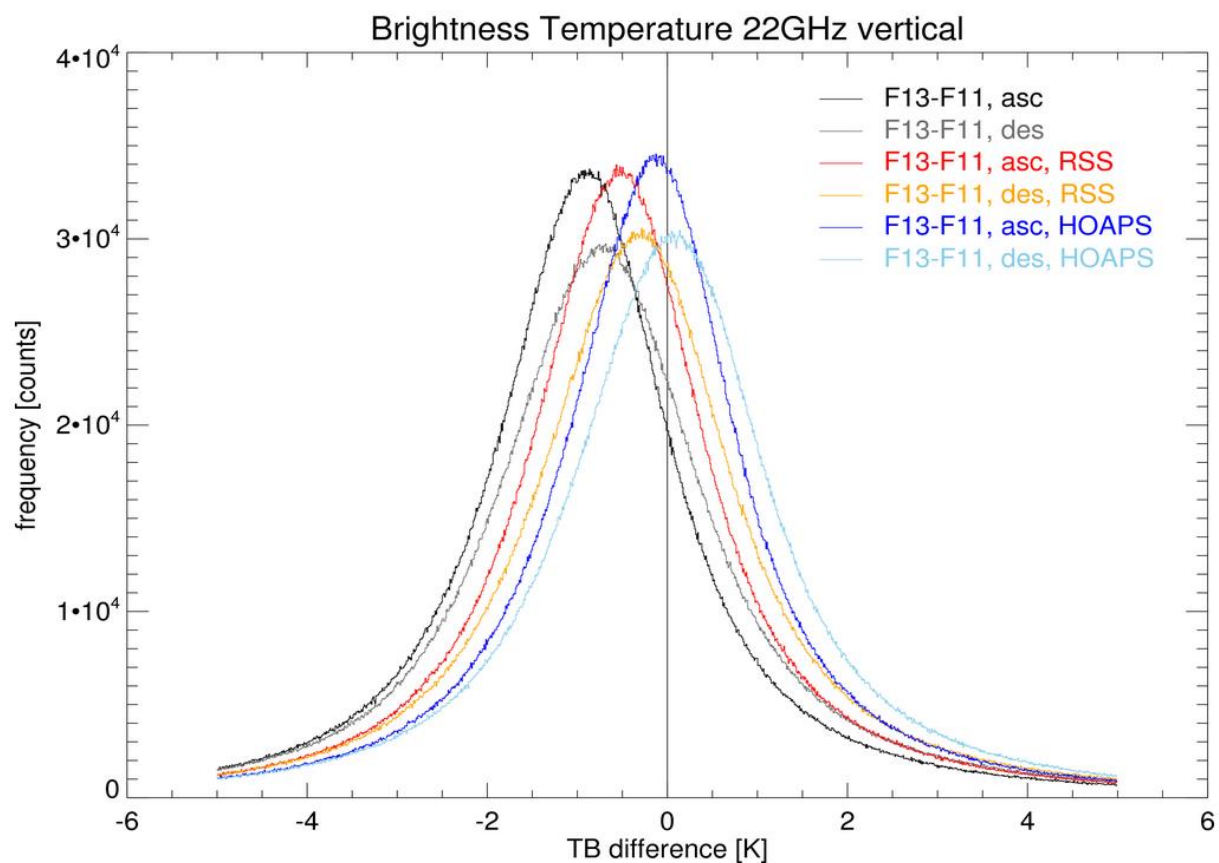


**Figure III-10:** Histograms of brightness temperature differences at 22 GHz between F13 and F11 before inter-calibration (black and grey) and after inter-calibration and EIA normalisation offsets are applied (dark blue, light blue). The brightness temperature differences from the RSS version 6 data record (red and orange) are shown for reference (no EIA offsets applied).

For each radiometer, a match-up data set with the selected reference radiometer (or transfer standard) is compiled from the collocated gridded mean TBs for the entire overlap period. The calibration coefficients are then fitted to the inter-calibration model (equation III-14) using the EIA and local time normalized TB pairs from both radiometers as input, while merging ascending and descending orbits to further minimize the influence of remaining diurnal cycle variations.

The derived scaling factors, offsets and non-linearity coefficients are summarized in Table III-4 in Appendix A. As an example for the successful homogenisation procedure histograms of brightness temperature differences between F13 and F11 for the 22 GHz channel are shown in Figure III-10. Before the offsets are applied the mean difference is about 1 K and after the inter-calibration and EIA normalisation offsets are applied the mean difference is significantly reduced to about 0.1 K.

Due to the accurate and stable in-orbit calibration of the SSM/I, the coefficients are considered to be constant during the lifetime of a radiometer (Colton and Poe, 1999) and are used to homogenize the measurements of different SSM/I instruments. The inter-calibration offsets  $\Delta T_{ICAL}$  to the brightness temperatures are assumed to be valid over all surface types and computed during the final processing for each FOV and then separately archived in the FCDR data files:

$$\Delta T_{ICAL} = T_B'' - T_B \cdot \quad \text{Equation III-16}$$

By keeping the incidence angle normalisation TB offsets and the inter-calibration TB offsets separately from the TBs itself, each user has the freedom to choose whatever correction or combination is sufficient for their application. If a geophysical retrieval algorithm assumes a fixed Earth incidence angle the final brightness temperature at the nominal EIA over water surfaces is:

$$T_B''(\theta = 53^\circ) = T_B(\theta) + \Delta T_{EIA} + \Delta T_{ICAL} \cdot \quad \text{Equation III-17}$$

However, if the retrieval accounts for the Earth incidence angle the final brightness temperature would be:

$$T_B'(\theta) = T_B(\theta) + \Delta T_{ICAL} \cdot \quad \text{Equation III-18}$$

while passing the EIA to the retrieval procedure. As the incidence angle normalisation TB offsets are only available over water, geophysical retrievals over land and ice should always account for varying EIA within their procedures.

## 4.7 Error Budget Estimates

A complete error analysis for the SSM/I brightness temperatures is a very challenging task as it requires careful and fully documented pre-launch measurements of all components, subsystems and of the final fully integrated system simulating expected orbital conditions. However, due to the military heritage of the SSM/I not all information about the instrument is available. Moreover, according to Colton and Poe (1999), ground measurements for the calibrations test are believed to contain artefacts of the test setup which do not allow us to use

the derived calibration correction for on-orbit data. Therefore only an estimate of the expected error budget and the contributing terms can be derived.

The total expected error of a quantity can be divided into two components: a systematic error (accuracy) and a random error (precision). While the random error of the TBs can be determined on-orbit from the instrument measurements used to calibrate the radiometer, the total systematic error must be identified during the ground measurements. Following the ISO Guide to the expression of uncertainties (ISO GUM) the random errors can be evaluated by statistical methods and are therefore Type A uncertainties. The systematic errors must be estimated from prelaunch measurements or validation activities and thus are Type B uncertainties.

#### 4.7.1 Random Error

The precision of a radiometer is usually expressed as a noise equivalent temperature  $NE\Delta T$ , which is the standard uncertainty of the measurement. This uncertainty is defined as the standard deviation of the radiometer referenced to the energy of the radiation incident on the antenna. This noise can be estimated using the SSM/I on-orbit calibration measurements and the calibration equation (see also section 4.3). Applying a standard error propagation to equation (III-5).

$$T_A = \frac{\langle T^H \rangle - T^C}{\langle C^H \rangle - \langle C^C \rangle} \cdot C^E + \frac{T^C \cdot \langle C^H \rangle - \langle T^H \rangle \cdot \langle C^C \rangle}{\langle C^H \rangle - \langle C^C \rangle} \quad \text{Equation III-19}$$

yields

$$NE\Delta T^2 = \underbrace{\left( \frac{\delta T_A}{\delta \langle T^H \rangle} \cdot \sigma_{\langle T^H \rangle} \right)^2}_{s(T^H)} + \underbrace{\left( \frac{\delta T_A}{\delta \langle C^H \rangle} \cdot \sigma_{\langle C^H \rangle} \right)^2}_{s(C^H)} + \underbrace{\left( \frac{\delta T_A}{\delta \langle C^C \rangle} \cdot \sigma_{\langle C^C \rangle} \right)^2}_{s(C^C)} + \underbrace{\left( \frac{\delta T_A}{\delta C^E} \cdot \sigma_{C^E} \right)^2}_{s(C^E)} \quad \text{Equation III-20}$$

with the following standard uncertainties contributing to the combined standard variability:

- Standard uncertainty due to noise in the smoothed temperature readings  $\sigma_{\langle T^H \rangle}$ :

$$s(T^H) = \frac{C^E - \langle C^C \rangle}{\langle C^H \rangle - \langle C^C \rangle} \cdot \sigma_{\langle T^H \rangle} \quad \text{Equation III-21}$$

- Standard uncertainty due to noise in the smoothed hot counts  $\sigma_{\langle C^H \rangle}$ :

$$s(C^H) = \frac{[\langle T^H \rangle - T^C] \cdot [\langle C^C \rangle - C^E]}{[\langle C^H \rangle - \langle C^C \rangle]^2} \cdot \sigma_{\langle C^H \rangle} \quad \text{Equation III-22}$$

- Standard uncertainty due to noise in the smoothed cold counts  $\sigma_{\langle C^C \rangle}$ :

$$s(C^C) = \frac{[\langle T^H \rangle - T^C] \cdot [C^E - \langle C^H \rangle]}{[\langle C^H \rangle - \langle C^C \rangle]^2} \cdot \sigma_{\langle C^C \rangle} \quad \text{Equation III-23}$$

- Standard uncertainty due to noise in the Earth counts  $\sigma_{C^E}$ :

$$s(C^E) = \frac{\langle T^H \rangle - T^C}{\langle C^H \rangle - \langle C^C \rangle} \cdot \sigma_{C^E} \quad \text{Equation III-24}$$

The standard deviations of the smoothed cold counts, smoothed hot counts and smoothed temperature readings are estimated from all available valid observations on a daily basis. The daily mean noise equivalent temperature  $NE\Delta T$  for each channel can then be estimated while viewing the hot target, i.e. replacing  $C^E$  with  $C^H$ . As the variability of the hot counts is larger than the variability of the cold counts this value is a valid estimate for the maximum expected  $NE\Delta T$ .

The term with the largest contribution to the combined standard uncertainty is the uncertainty due to noise in the Earth counts  $E(C^E)$  with about 98%. The contribution from the uncertainty in the temperature readings can be neglected while the uncertainty in the cold and hot target readings contribute the remaining 2%. The across-scan smoothing applied to the scanline mean values (equation III-3) reduces  $NE\Delta T$  by approximately 10%.


The estimated variances of the smoothed cold counts, smoothed hot counts, smoothed hot target temperature and the noise equivalent temperature are archived in the FCDR data files as daily mean values.

#### 4.7.2 Systematic Error

As noted above, it is not possible to specify a complete systematic error for the SSM/I brightness temperatures. Apart from the aforementioned limitations to trace observed systematic differences back to SI standards, there is a more general problem in obtaining an accurate standard for comparison with the SSM/I observations (Hollinger, 1990). There are no absolute reference observations available to validate the absolute calibration because the SSM/I is a unique observing system. This means the SSM/I brightness temperatures can only be compared against similar observations, for example aircraft measurements with an SSM/I simulator, or against simulated brightness temperatures from a radiative transfer model.

Both methods have been used to evaluate the absolute calibration of the SSM/I during the F08 instrument cal/val program (Hollinger, 1990). The conclusion from these evaluation experiments is that the absolute calibration shows no significant systematic bias and may be better than the uncertainty of its determination of  $\pm 3$  K.

The total radiometer calibration error budget is composed of the following contributors: (a) hot load reference error, (b) cosmic background reference error, (c) radiometer/calibration nonlinearity, (d) radiative coupling  $\epsilon$  uncertainty, and (e) errors in the APC coefficients. An

	<b>Algorithm Theoretical Basis Document</b> <b>Microwave Imager Radiance FCDR R4</b> <b>SSM/I Brightness Temperatures</b>	Doc. No: SAF/CM/DWD/ATBD/FCDR_SSM/I Issue: 2.2 Date: 2022-01-31
---	---	---

analysis of these error terms has been done by Hollinger (1989) and Colton and Poe (1999) with the following results:

*a) Hot load reference error*

The calibration error of the hot load was determined pre-launch by comparison with a variable precision calibration reference target over a range of 100 K to 375 K during thermal vacuum calibration. These tests show no systematic calibration error (Hollinger, 1989).

*b) Cosmic background reference error*

An analysis of the calibration reflector antenna patterns when the SSM/I is in the calibration position reveals that the reception of Earth and spacecraft radiation is extremely small (less than a few tenth of a degree). Thus it is believed that the SSM/I calibration reflector provides a clear view of the cosmic background to the feedhorn and hence provides a highly accurate blackbody calibration reference (Hollinger, 1989). However, this is not the case during phases when parts of the moon are in the field of view of the reflector (see section 4.4.2). This short-lived intrusion events can cause an underestimation of the true scene temperature of up to 0.5 K, depending on the channel and scene temperature.

*c) Radiometer/calibration nonlinearity*

Nonlinearities in the calibration measurements and in the radiometer receiver may be expected to appear in the calibration data. At measurement temperatures equal to the calibration reference targets, the calibration uncertainty is the accuracy of the reference, which does not show a systematic error (see above). At intermediate temperatures, radiometer nonlinearity and calibration reference temperature errors contribute to the total uncertainty with the errors weighted according to the temperature difference between the input and the calibration references. To test the radiometer absolute calibration, thermal vacuum tests have been conducted. Calibration cycles were run for three different sensor temperatures: cold (0°C), ambient (28°C) and hot (38°C). For the on-orbit expected operating range the calibration errors are typically -1.4 to 0.5 K (Colton and Poe, 1999) and hence within the instrument specifications. The images point to a scene temperature dependent bias with a larger underestimation for colder scene temperatures. However, the measurements are believed to contain artefacts due to the actual test setup. The on-orbit calibration are expected to perform better than the pre-launch calibration tests indicate.

*d) Radiative coupling  $\epsilon$  uncertainty*

The radiative coupling coefficient  $\epsilon$  (see section 4.3) was originally determined for the SSM/I on F08 and was used unchanged in the computation of the antenna temperatures since then. The correction due to this factor depends on the temperature difference between the hot load and the forward radiator plate. This correction is typically in the order of 0.1 K for an expected temperature difference of 10 K. However, some instruments show a very strong seasonal variation in the temperature difference reaching 40 K. A relative uncertainty of 1% in  $\epsilon$  can then lead to an uncertainty of 0.4 K in the scene brightness temperature.

*e) Errors in the APC coefficients*

During the ground instrument calibration also a radiometric characterization of the antenna properties is performed. The performance was established from analyses of the antenna gain function as measured on an antenna range from which, amongst others, feedhorn spillover

and cross-polarization loss are determined. The accuracy of the derived APC coefficients is a function of the number of antenna range measurements, the dynamic range of the measurements, as well as the repeatability, accuracy, and stability of the antenna range transmitter/receiver over the measurement period. The estimated absolute accuracy of the feedhorn spillover is 0.3-0.5% and the relative cross-polarization accuracy is in the order of 5-10% (Colton and Poe, 1999). The uncertainty in the spillover translates to a scene dependent uncertainty in the order of about 1-1.5 K at 300 K scene temperature. The uncertainty in the cross-polarization accuracy results in an uncertainty which depends on the scene polarization difference in the order of 0.15-0.3 K for 50 K scene polarization.

The individual systematic error contributions are summarized in Table III-5. The standard uncertainties  $u$  of the error terms  $y$  are estimated assuming a uniform distribution for a minimum and a maximum expected range of variation  $\Delta a$  (as estimated above):

$$u(y) = \frac{\Delta a}{\sqrt{3}} \quad \text{Equation III-25}$$

The combined expected standard uncertainty of the systematic error

$$u_c(T_B) = \sqrt{\sum_i u_i^2(y)} \quad \text{Equation III-26}$$

is then in the order of 0.6 —1 K, with a significant dependence on the scene temperature (nonlinearity and spillover terms) and a minor dependence on the scene polarization.

## 4.8 Practical Considerations

### 4.8.1 Validation

A conclusion from the error budget estimation (see section 4.7) is that a complete comprehensive validation of the SSM/I brightness temperatures is not possible. The final aim of an evaluation process must be to show that the measured SSM/I brightness temperatures are in agreement with modelled brightness temperatures within the expected random uncertainties. However, as a major requisite, a Fundamental Climate Data Record must show an improved quality compared to the existing raw data records in order to be a useful dataset providing an added value to the user community.

In a first step this FCDR of SSM/I brightness temperatures will be compared to the original raw data records and to other existing FCDRs, e.g. from CSU and RSS, in order to quantify the quality of the inter-sensor calibration and to compare the different inter-sensor approaches over different surface types and to evaluate the temporal stability. Also an evaluation of observed minus simulated brightness temperatures using the ERA-5 reanalysis will be carried out. It is also envisaged to analyse the feedback files from the ERA-5 reanalysis system because the CM SAF SSM/I FCDR has been assimilated in this version. The feedback files can be used to quantify remaining issues and evaluate the observed differences.

#### 4.8.2 Quality control

The original SSM/I raw data records do not contain any quality control (QC) flags. The calibration data is analysed to filter the raw data records and assign the following quality flags:

- The calibration temperature quality is tested and an overall calibration QC flag is set, when
  - the hot load temperature is out of bounds ( $230\text{ K} < T^{HL} < 330\text{ K}$ ),
  - the absolute difference between any hot load temperature reading and the scan-line mean is larger than 0.5 K,
  - the absolute difference between the mean hot load temperature and the forward radiator temperature is larger than 80 K,
  - the absolute difference between the mean hot load temperature and the R.F. mixer temperature is larger than 80 K,
  - the absolute difference between the forward radiator temperature and the R.F. mixer temperature is larger than 160 K.
- All channel calibration data is tested and a channel QC flag is set, when
  - the gain control settings differ between A and B scan,
  - the cold counts are out of bounds ( $200 < C^C < 2500$ ),
  - the hot counts are out of bounds ( $1500 < C^H < 3400$ ),
  - the difference between any  $C^C$  or  $C^H$  and the scan-line mean value is larger than 20.
- All FOV brightness temperatures are tested and a FOV channel QC flag is set when
  - the TB is out of bounds:  $130\text{ K} < 19v, 22v, 37v, 85v < 310\text{ K}$ ;  $80\text{ K} < 19h < 300\text{ K}$ ;  $110\text{ K} < 37h, 85h < 300\text{ K}$ ;
  - the TB difference between vertical and horizontal polarisation is out of bounds:  $TBv - TBh < -20\text{ K}$ .
- If more than 10 FOVs in the lower-resolution channels or more than 20 FOVs in higher-resolution channels are flagged the whole scan line is regarded as bad quality and the overall calibration QC flag is set.

All scan lines remain in the file, so every user has the freedom to apply their own quality tests or to use the supplied quality flags to filter non valid data.

#### 4.8.3 Outputs (FCDR Product Definition)

The CM SAF FCDR from SSM/I brightness temperatures are compiled as daily collections of all observations from one sensor. Organizing the data records in files with fixed start and end times simplifies the usage in climatological applications. The data files are archived in NetCDF format following NetCDF Climate and Forecast (CF) Metadata Convention version 1.7 (<http://cf-pcmdi.llnl.gov/documents/cf-conventions/1.7/cf-conventions.html>). All sensor specific data available in the raw data records are provided as well as additional information like quality control flags, Earths incidence angles, averaged 85 GHz brightness temperatures, incidence angle normalisation offsets and inter-sensor calibration offsets. A detailed description of the product files is given in the Product User Manual (PUM, RD 3).

## 5 Assumptions and Limitations

The inter-sensor calibration method used here to homogenize the SSM/I brightness temperature time series (see section 4.6.2) does not account for an absolute radiometric offset. The reference target is the SSM/I aboard DMSP F11, which means that any absolute offset in the F11 TBs will be transferred to the other radiometers. However, one reason to choose the F11 as the reference target was a good performance when validating against collocated in-situ wind speed measurements from buoy observations. This should at least minimize the remaining absolute error in the brightness temperature data record.

The inter-sensor calibration is determined over ocean, sea-ice and cold scenes over land because of a lower variability, smaller diurnal cycle and better behaved error characteristics. Due to this restriction not the complete range of possible TBs is covered for all channels. It is assumed that the inter-sensor differences can be characterized as a linear problem and the derived correction coefficients can be used over land and ice as well.

The incidence angle normalisation TB offsets (see section 4.6.1) are only available over water. Geophysical retrievals over land and ice should always account for varying EIAs within their procedures.

During the time period from April 1988 to December 1991, the 85 GHz channel on DMSP F08 are defective. A replacement algorithm has been developed to estimate the 85 GHz measurements from the lower frequencies (see section 4.5.2). However, this reconstruction is limited to the variability observed in the lower frequencies and can not fully recover the missing 85 GHz channel characteristics. Over land and ice surfaces this general approach is not applicable due to the strongly varying surface emissivity.

## 6 Implications for Future Mission Specification and Instrument Design

From the identified issues affecting the performance and quality of the SSM/I measurements important implications for future microwave imagers can be drawn aiming to ensure and improve the usability of the data records in climate applications:

- Extensive pre-launch measurements to characterize the systematic uncertainties of the instrument following SI standards and to specify the radiometer absolute calibration,
- Determination of the radiometer calibration non-linearity,
- Improved shielding and design of the instruments cold and warm calibration targets,
- Improved geolocation (including EIA) and platform stability (attitude corrections, orbit corrections),
- Open access to all necessary documentation, e.g. instrument design, pre-launch measurements, spacecraft orbit elements, and on-orbit performance data.

## 7 References

Andersson, Axel; Bakan, Stephan; Fennig, Karsten; Grassl, Hartmut; Klepp, Christian-Phillip; Schulz, Joerg, 2007: Hamburg Ocean Atmosphere Parameters and Fluxes from Satellite Data - HOAPS-3 - monthly mean., electronic publication, World Data Center for Climate, doi:10.1594/WDCC/HOAPS3\_MONTHLY.

Andersson, Axel; Bakan, Stephan; Fennig, Karsten; Grassl, Hartmut; Klepp, Christian-Phillip; Schulz, Joerg, 2007: Hamburg Ocean Atmosphere Parameters and Fluxes from Satellite Data - HOAPS-3 - 5-days mean., electronic publication, World Data Center for Climate, doi:10.1594/WDCC/HOAPS3\_PENTAD.

Andersson, Axel; Bakan, Stephan; Fennig, Karsten; Grassl, Hartmut; Klepp, Christian-Phillip; Schulz, Joerg, 2007: Hamburg Ocean Atmosphere Parameters and Fluxes from Satellite Data - HOAPS-3 - twice daily composite., electronic publication, World Data Center for Climate, doi:10.1594/WDCC/HOAPS3\_DAILY.

Andersson, A., Fennig, K., Klepp, C., Bakan, S., Graßl, H., and Schulz, J.: The Hamburg Ocean Atmosphere Parameters and Fluxes from Satellite Data – HOAPS-3, Earth Syst. Sci. Data, 2, 215-234, doi:10.5194/essd-2-215-2010, 2010.

Andersson, A., C. Klepp, K. Fennig, S. Bakan, H. Graßl, and J. Schulz: Evaluation of HOAPS-3 ocean surface freshwater flux components, Journal of Applied Meteorology and Climatology, 50, 379-398, doi:10.1175/2010JAMC2341.1, 2011

Berg, W., Sapiano, M. R. P. ; Horsman, J. ; Kummerow, C., 2012: Improved Geolocation and Earth Incidence Angle Information for a Fundamental Climate Data Record of the SSM/I Sensors, IEEE Transactions on Geoscience and Remote Sensing, Early online release, doi: 10.1109/TGRS.2012.2199761

Colton, M. C. and Poe, G. A.: Intersensor Calibration of DMSP SSM/I's: F-8 to F-14, 1987–1997, IEEE Trans. Geosci. Remote Sens., 37, 418–439, 1999.


Fennig, Karsten; Bakan, Stephan; Grassl, Hartmut; Klepp, Christian-Phillip; Schulz, Joerg, 2006: Hamburg Ocean Atmosphere Parameters and Fluxes from Satellite Data - HOAPS II - monthly mean., electronic publication, WDCC, doi:10.1594/WDCC/HOAPS2\_MONTHLY.

Fennig, Karsten; Bakan, Stephan; Grassl, Hartmut; Klepp, Christian-Phillip; Schulz, Joerg, 2006: Hamburg Ocean Atmosphere Parameters and Fluxes from Satellite Data - HOAPS II - 5-days mean., electronic publication, WDCC, doi:10.1594/WDCC/HOAPS2\_PENTAD.

Fennig, K., Schröder, M., Andersson, A., and Hollmann, R.: A Fundamental Climate Data Record of SMMR, SSM/I, and SSMIS brightness temperatures, Earth Syst. Sci. Data, 12, 647–681, <https://doi.org/10.5194/essd-12-647-2020>, 2020.

Furhop, R. and Simmer, C.: SSM/I Brightness Temperature Corrections for Incidence Angle Variations, J. Atmos. Oceanic Technol., 13, 246–254, 1996.

GLOBE Task Team: The Global Land One-kilometer Base Elevation (GLOBE) Digital Elevation Model, Version 1.0., Tech. Rep., National Oceanic and Atmospheric Administration,

	<b>Algorithm Theoretical Basis Document</b> <b>Microwave Imager Radiance FCDR R4</b> <b>SSM/I Brightness Temperatures</b>	Doc. No: SAF/CM/DWD/ATBD/FCDR_SSM Issue: 2.2 Date: 2022-01-31
---	---	---

National Geophysical Data Center, 325 Broadway, Boulder, Colorado 80303, USA, <http://www.ngdc.noaa.gov/mgg/topo/globe.html>, 1999.

Hollinger, J., Poe, G..A.: Special Sensor Microwave/Imager User's Guide, Naval Research Laboratory Report, Washington DC, 1987

Hollinger, J.: DMSP Special Sensor Microwave/Imager Calibration/Validation I, Naval Research Laboratory, Washington, DC 20375-5000, 1989

Hollinger, J. P., Peirce, J. L., and Poe, G. A.: SSM/I Instrument Evaluation, IEEE Trans. Geosci. Remote Sens., 28, 781–790, 1990.

Hoots, F. R., Roehrich, L. R.: "Models for Propagation of NORAD Element Sets", December 1988

Kunkee, D. B., Poe, G. A, Savage, R., and Peirce, J: Special Sensor Microwave Imager Sounder (SSMIS) Radiometric Calibration Anomalies – Part I: Identification and Characterization, IEEE Trans. Geosci. Remote Sens., 46, 1017-1033, 2008

Njoku, E. G. (2003): Nimbus-7 SMMR Pathfinder Brightness Temperatures, Version 1., Boulder, Colorado USA. NASA National Snow and Ice Data Center Distributed Active Archive Center. DOI:10.5067/7Y1XWXT07HH8.

O'Dell, Christopher W., Frank J. Wentz, Ralf Bennartz, 2008: Cloud Liquid Water Path from Satellite-Based Passive Microwave Observations: A New Climatology over the Global Oceans. J. Climate, 21, 1721–1739. doi: <http://dx.doi.org/10.1175/2007JCLI1958.1>

Poe, G. A. and Conway R. W.: A Study of the Geolocation Errors of the Special Sensor Microwave/Imager (SSM/I), IEEE Trans. Geosci. Remote Sens., 28, 791–799, 1990.

Poli, P.; Peubey C., Fennig K., Schröder M., Roebelling R., Geer A. (2015): Pre-assimilation feedback on a Fundamental Climate Data Record of brightness temperatures from Special Sensor Microwave Imagers: A step towards MIPs4Obs?, ERA Report Series, 19.


Ritchie, A. A., Smith, M. R., Goodman, H. M., Schudalla, R. L., Conway, D. K., LaFontaine, F. J., Moss, D., and Motta, B.: Critical Analyses of Data Differences Between FNMOC and AFGWC Spawned SSM/I Datasets, J. Atmos. Sci., 55, 1601–1612, 1998.

Semunegus, H., Berg, W., Bates, J. J., Knapp, K. R., Kummerow, C.: An Extended and Improved Special Sensor Microwave Imager (SSM/I) Period of Record, Journal of Applied Meteorology and Climatology, 49, 424-436, 2010

Semunegus, H: Remote Sensing Systems Version-6 Special Sensor Microwave/Imager Fundamental Climate Data Record, Climate Algorithm Theoretical Basis Document, Climate Data Record (CDR) Program, CDRP-ATBD-0100, 2011

Swift, C. T., Fedor, L. S., and Ramseier, R. O.: An Algorithm to Measure Sea Ice Concentration with Microwave Radiometers, J. Geophys. Res.-Oceans, 90, 1087–1099, 1985.

Wentz, F. J.: User's Manual for SSM/I Antenna Temperature Tapes Revision 1, Technical Report 120191, Remote Sensing Systems, Santa Rosa, California, 1991.

	<b>Algorithm Theoretical Basis Document</b> <b>Microwave Imager Radiance FCDR R4</b> <b>SSM/I Brightness Temperatures</b>	Doc. No: SAF/CM/DWD/ATBD/FCDR_SSMI Issue: 2.2 Date: 2022-01-31
---	---	--

Wentz, F. J.: Production of SSM/I Data Sets, Technical Report 90192, Remote Sensing Systems, Huntsville, Alabama, 1992.

## 8 Appendix A

**Table III-1:** DMSP SSM/I orbit and sensor specific information.

	F08	F10	F11	F13	F14	F15
<b>Launch date</b>	1987-06-18	1990-12-01	1991-11-28	1995-03-24	1997-04-04	1999-12-12
<b>Altitude range [km]</b>	832 - 851	728 – 841	841 – 878	839 – 884	837 – 884	833 - 877
<b>Pitch correction</b>	-0.11	0.19	0.04	0.14	0.12	0.08
<b>Roll correction</b>	0.10	-0.09	-0.01	-0.10	-0.07	0.00
<b>Yaw correction</b>	-0.60	0.10	-0.25	-0.10	-0.65	0.20
<b>Elevation offset</b>	0.18	-0.04	0.00	0.36	0.25	0.39
<b>Warm target emission</b>	0.9905	0.9940	0.9940	0.9950	0.9800	0.9900

**Table III-2:** Antenna spillover and polarisation leakage factors (Wentz, 1991).

	19v	19h	22v	37v	37h	85v	85h
<b>Spillover <math>\delta</math></b>	0.03199	0.03199	0.02685	0.01434	0.01434	0.01186	0.01186
<b>Leakage <math>\chi_p</math></b>	0.00379	0.00525	0.00983	0.02136	0.02664	0.01387	0.01967

**Table III-3:** Calibration across-scan smoothing weights for hot and cold target counts and estimated resulting effective correlation of smoothed calibration coefficients.

<b>Scan Offset</b>	<b>Effective Weight</b>	<b>Effective Correlation</b>
<b>0</b>	0.1612	1.0000
<b>± 1</b>	0.1493	0.9594
<b>± 2</b>	0.1186	0.8494
<b>± 3</b>	0.0807	0.6916
<b>± 4</b>	0.0472	0.5152
<b>± 5</b>	0.0236	0.3482

**Table III-4:** Inter-sensor scaling factors a, calibration offsets b and non-linear coefficients c.

		19 GHz, v	19 GHz, h	22 GHz, v	37 GHz, v	37 GHz, h	85 GHz, v	85 GHz, h
<b>F08</b>	a	0.99282	0.99360	1.00015	1.00223	1.00160	1.00000	1.00000
	b	1.953	1.658	0.121	-0.061	0.039	0.850	0.430
	c	-1.08E-05	2.24E-05	-1.64E-05	-0.54E-05	-0.35E-05	0.00E-05	0.00E-05
<b>F10</b>	a	0.98983	0.99224	0.99941	0.99872	0.99826	1.00343	1.00353
	b	1.832	1.565	0.005	-0.169	0.016	0.143	-0.265
	c	-0.30E-05	2.23E-05	-1.35E-05	0.16E-05	0.00E-05	-0.62E-05	-0.32E-05
<b>F11</b>	a	1.00000	1.00000	1.00000	1.00000	1.00000	1.00000	1.00000
	b	0.000	0.000	0.000	0.000	0.000	0.000	0.000
	c	-0.87E-05	-1.09E-05	0.22E-05	-0.51E-05	0.46E-05	0.03E-05	0.26E-05
<b>F13</b>	a	0.99388	0.99675	1.00073	1.00028	0.99964	1.00376	1.00444
	b	1.674	0.858	0.068	-0.075	0.273	-0.023	-0.172
	c	2.05E-05	2.23E-05	1.06E-05	-0.68E-05	1.86E-05	1.58E-05	1.16E-05
<b>F14</b>	a	0.99371	0.99578	1.00063	0.99849	0.99819	1.00247	1.00343
	b	1.579	1.060	0.152	0.156	-0.056	0.129	0.053
	c	0.74E-05	1.33E-05	0.19E-05	1.04E-05	-1.62E-05	-0.51E-05	-0.61E-05
<b>F15</b>	a	0.99297	0.99489	1.00088	0.99998	0.99926	1.00332	1.00403
	b	2.000	1.553	-0.008	0.099	-0.283	0.176	-0.020
	c	0.55E-05	3.92E-05	0.29E-05	0.80E-05	-2.28E-05	-0.86E-05	-0.51E-05

**Table III-5:** Summary of estimated systematic error source contributions.


Systematic error source	Systematic error [K]	Standard uncertainty [K]
Hot load reference	-	-
Cosmic background reference *	-	-
Calibration non-linearity	-1.40 – 0.50	0.15 – 0.40
Radiative coupling	0.10 – 0.40	0.06 – 0.25
Cross polarization (APC coefficients)	0.15 – 0.30	0.10 – 0.20
Feedhorn spillover (APC coefficients)	1.00 – 1.50	0.60 – 0.90

(\*) no moonlight intrusion events

## 9 Glossary

APC	Antenna Pattern Correction
ATBD	Algorithm Theoretical Baseline Document
CM SAF	Satellite Application Facility on Climate Monitoring
DMSP	Defense Meteorological Satellite Program
DWD	Deutscher Wetterdienst (German MetService)
ECI	Earth-centred inertial
ECMWF	European Centre for Medium Range Forecast
ECV	Essential Climate Variable
EIA	Earth Incidence Angle
EPS	European Polar System
EUMETSAT	European Organisation for the Exploitation of Meteorological Satellites
FCDR	Fundamental Climate Data Record
FMI	Finnish Meteorological Institute
FOV	Field of view
GCOS	Global Climate Observing System
GLOBE	The Global Land One-kilometer Base Elevation
HOAPS	The Hamburg Ocean Atmosphere Fluxes and Parameters from Satellite data
IOP	Initial Operations Phase
KNMI	Koninklijk Nederlands Meteorologisch Instituut
MD5	Message-Digest Algorithm 5
MSG	Meteosat Second Generation
NASA	National Aeronautics and Space Administration
NCEP	National Centers for Environmental Prediction
NDBC	National Data Buoy Center
NESDIS	National Environmental Satellite, Data, and Information System
NMHS	National Meteorological and Hydrological Services
NOAA	National Oceanic & Atmospheric Administration

NWP	Numerical Weather Prediction
PRD	Product Requirement Document
PUM	Product User Manual
QC	Quality Control
RMIB	Royal Meteorological Institute of Belgium
RMS	Root Mean Square
RSS	Remote Sensing Systems
SAF	Satellite Application Facility
SI	Système international d'unités
SMHI	Swedish Meteorological and Hydrological Institute
SMMR	Scanning Multichannel Microwave Radiometer
SSM/I	Special Sensor Microwave Imager
SSMIS	Special Sensor Microwave Imager Sounder
TA	Antenna Temperature
TB	Brightness Temperature
TDR	Temperature Data Records

	<b>Algorithm Theoretical Basis Document</b> <b>Microwave Imager Radiance FCDR R4</b> <b>SSM/I Brightness Temperatures</b>	Doc. No: SAF/CM/DWD/ATBD/FCDR_SSMI Issue: 2.2 Date: 2022-01-31
---	---	--

## IV SSMIS

The algorithms and methods to build the SSMIS FCDR component are described in the corresponding ATBD [RD 2]. The fourth release will include four additional years (2016-2020) of SSMIS observations from F16, F17, and F18.